



The
University
Of
Sheffield.

This is a repository copy of *Labile low-valent tin azides: syntheses, structural characterization, and thermal properties..*

White Rose Research Online URL for this paper:

<https://eprints.whiterose.ac.uk/125487/>

Version: Supplemental Material

Article:

Campbell, R., Konar, S., Hunter, S. et al. (2 more authors) (2018) Labile low-valent tin azides: syntheses, structural characterization, and thermal properties. Inorganic Chemistry, 57 (1). pp. 400-411. ISSN 0020-1669

<https://doi.org/10.1021/acs.inorgchem.7b02621>

This document is the Accepted Manuscript version of a Published Work that appeared in final form in Inorganic Chemistry, copyright © American Chemical Society after peer review and technical editing by the publisher. To access the final edited and published work see <https://doi.org/10.1021/acs.inorgchem.7b02621>

Reuse

Items deposited in White Rose Research Online are protected by copyright, with all rights reserved unless indicated otherwise. They may be downloaded and/or printed for private study, or other acts as permitted by national copyright laws. The publisher or other rights holders may allow further reproduction and re-use of the full text version. This is indicated by the licence information on the White Rose Research Online record for the item.

Takedown

If you consider content in White Rose Research Online to be in breach of UK law, please notify us by emailing eprints@whiterose.ac.uk including the URL of the record and the reason for the withdrawal request.

Supporting Information

Labile Low-Valent Tin Azides: Syntheses, Structural Characterisation, And Thermal Properties

Rory Campbell,^[a] Sumit Konar,^[b] Steven Hunter,^[b] Colin Pulham,*^[b] Peter Portius*^[a]

^[a]Department of Chemistry, University of Sheffield, Brook Hill, S3 7HF, U.K.

Email: p.portius@sheffield.ac.uk

^[b]School of Chemistry, University of Edinburgh, David Brewster Rd., EH9 3FJ, U.K.

Table of Contents

1. General Experimental Procedures.....	3
2. Single Crystal X-Ray Diffraction Data.....	5
Figure S1. Unit cell of $\text{Sn}(\text{N}_3)_2(\text{py})_2$ (2) viewed along the <i>b</i> -axis, with ellipsoids at the 50 % probability level.	5
Figure S2. Unit cell packing of $\text{Sn}(\text{N}_3)_2(\text{pic})_2$ (3) showing the ‘dimeric’ interaction between two neighbouring Sn–N _a units.	5
Figure S3. Still image captured of guanidinium triazidostannate (4) crystals under a microscope showing evolution of HN_3 caused by moisture in the nujol.....	6
Figure S4. ORTEP diagram showing the graph sets assigned to hydrogen bonds in the structure of guanidinium triazidostannate (4).	6
Figure S5. Thermal ellipsoid drawing (50 % probability level) of the unit cell content and intermolecular contacts shorter than the sum of the vdW radii in the crystal of compound 4 at 100 K. H atoms are drawn with a radius of 0.2 Å.....	7
Table S1. Hydrogen bond geometries in the crystal structure of guanidinium triazidostannate (4) at 100 K.....	7
Table S2. Second level graph set matrix for the hydrogen bond network in guanidinium triazidostannate (4).	7
2.1 Diazidobis(pyridine)tin (2)	8
2.2 Diazidobis(4-picoline)tin (3).....	8
2.3 Guanidinium triazidostannate (4).....	9
3. Powder Diffraction Data	10
Table S3. Atomic positions in the structure of $\text{Sn}(\text{N}_3)_2$ (1) determined by PXRD, expressed as fractional coordinates.....	10
Figure S6. (Top) 3D representation of the structure solution of $\text{Sn}(\text{N}_3)_2$ (1) determined by Rietveld refinement; (bottom) Overlay of the predicted vs. observed powder pattern with the subtraction result shown below	11

Table S4. Comparison of the geometries in the structures determined from DFT-D calculations compared to those derived from the Rietveld refinement of the PXRD data.....	11
Figure S7. Comparison with α -Zn(N ₃) ₂	12
4. Summary of crystal structure refinement parameters for tin(II) azides 1–4	12
Table S5. Summary of crystal structure refinement parameters for tin(II) azides 1–4.....	12
4.1 Ion volumes.....	14
Table S6. Unit cell volumes (V) of guanidinium and tetraphenylphosphonium salts.....	14
5. Density Functional Theory Calculations.....	15
6. Spectroscopic Data.....	16
6.1 FTIR Spectra.....	16
Figure S8. FTIR spectral series showing the effect of exposure of Sn(N ₃) ₂ (1) to air, which causes gradual shift to lower energy. The spectra are normalized to the $\nu_{as}(N_3)$ peak maximum.....	17
Figure S9. FTIR spectrum of Sn(N ₃) ₂ (py) ₂ (2) in pyridine solution showing the asymmetric azide stretch region.....	17
Figure S10. FTIR spectrum of Sn(N ₃) ₂ (pic) ₂ (3) in 4-picoline solution showing the asymmetric azide stretch region.....	18
Figure S11. FTIR spectrum of Sn(N ₃) ₂ (pic) ₂ (3) as a nujol suspension.....	18
Figure S12. FTIR spectra of guanidinium triazidostannate (4) in acetonitrile (black) and THF (red) solutions.....	19
6.2 NMR Spectra	20
Figure S14. ¹ H NMR of Sn(N ₃) ₂ (py) ₂ (2) in <i>d</i> ₅ -pyridine.....	20
Figure S15. Expanded view of the ¹ H NMR spectrum of Sn(N ₃) ₂ (py) ₂ (2) in <i>d</i> ₅ -pyridine	21
Figure S16. ¹³ C NMR spectrum of Sn(N ₃) ₂ (py) ₂ (2) in <i>d</i> ₅ -pyridine	21
Figure S17. ¹⁴ N NMR of Sn(N ₃) ₂ (py) ₂ (2) in <i>d</i> ₅ -pyridine	22
Figure S19. ¹ H NMR spectrum of Sn(N ₃) ₂ (pic) ₂ (3) in <i>d</i> ₅ -pyridine	23
Figure S20. Expanded view of the ¹ H NMR spectrum of Sn(N ₃) ₂ (pic) ₂ (3) in <i>d</i> ₅ -pyridine	23
Figure S21. ¹³ C NMR spectrum of Sn(N ₃) ₂ (pic) ₂ (3) in <i>d</i> ₅ -pyridine	24
Figure S22. ¹⁴ N NMR of Sn(N ₃) ₂ (pic) ₂ (3) in <i>d</i> ₅ -pyridine	24
Figure S23. ¹¹⁹ Sn NMR of Sn(N ₃) ₂ (pic) ₂ (3) in <i>d</i> ₅ -pyridine.....	25
Figure S24. ¹ H NMR of guanidinium triazidostannate (4) in CD ₃ CN	25
Figure S25. ¹³ C NMR (CPD) of guanidinium triazidostannate (4) in CD ₃ CN.....	26
Figure S25. ¹⁴ N NMR of guanidinium triazidostannate (4) in CD ₃ CN.....	26
Figure S26. ¹¹⁹ Sn NMR of guanidinium triazidostannate (4) in CD ₃ CN.....	27
7. Calorimetric and Thermogravimetric Data	27
Figure S27. Differential scanning calorimetry trace of diazidobis(pyridine)tin (2).....	27
Figure S28. Thermograms (3.80, 4.19 and 6.79 mg) of Sn(N ₃) ₂ (py) ₂ (2)	28
Figure S29. Differential thermograms derived from Fig. S28.....	28

Figure S30. DSC trace of $\text{Sn}(\text{N}_3)_2(\text{pic})_2$ (3)	29
Figure S31. Thermograms (5.55, 5.74, 6.38 mg) of $\text{Sn}(\text{N}_3)_2(\text{pic})_2$ (3)	29
Figure S32. Differential thermograms derived from Fig. S31	30
Figure S33. Differential scanning calorimetry traces of tin diazide (1).....	30
Figure S34. Differential scanning calorimetry trace of 4	31
8. References to the Literature	31

1. General Experimental Procedures

CAUTION: Tin(II) azide is a highly sensitive, explosive compound, and should be handled on a small scale with suitable safety precautions (face shield, Kevlar gloves, ear plugs, and protective clothing).

Manipulations involving compounds known (or suspected) to be air and/or moisture sensitive were performed using standard Schlenk, vacuum line, and glovebox techniques under an atmosphere of dry argon. The typical ultimate vacuum was around 4×10^{-2} mbar. Samples prepared for examination by spectroscopic and analytical methods were prepared in the glovebox whenever possible. During the preparation of samples of air or moisture sensitive solutions for Fourier transform infrared (FTIR) spectroscopy, a continuous low flow of argon was admitted *via* the sidearm of the Schlenk tube. A 1 ml glass piston pipette was purged in the argon stream five times then a sample was extracted, followed by a protective bubble of argon. The Specac cell was purged with argon for at least 30 s, before the sample was transferred (immediately) to the cell and the spectrum recorded promptly. Filtration of air and/or moisture sensitive compounds was achieved by the use of stainless steel filter canulas equipped with glass fibre filters secured by PTFE tape. Acetonitrile (Fisher, 99.9 %), and d₃-acetonitrile (Aldrich, 99.8 %), were dried over calcium hydride (Acros, 93 %) for 18 h, before trap-to-trap condensation. 4-picoline (Aldrich, 98 %), pyridine (Fisher Scientific, 99.8 %), pyridine-d₅ (Sigma Aldrich, 99.5 %) were dried over calcium hydride (Acros, 93 %) for 18 h, and vacuum distilled. Solvents were degassed, and stored under an argon atmosphere in suitably sized glass ampoules with a side inlet, which were sealed by J. Young's high vacuum greaseless stopcocks. Tin(II) fluoride (Sigma Aldrich, 99 %) and tin(II) chloride dihydrate (Sigma Aldrich, 98 %) were dried at 110 °C under vacuum for 16 h, TMS-N₃ was prepared by a published procedure.^[1] All dried solid reagents were stored in sealed vessels in a glovebox under an argon atmosphere. Infrared absorption spectra were recorded in the range 500–4000 cm⁻¹ on a Bruker Tensor 27 Fourier Transform Infrared (FTIR) spectrometer running the *Bruker OPUS* software package, or Bruker Alpha FTIR spectrometer running *Bruker OPUS 7.0*, at a spectral resolution of 2 cm⁻¹, either as a nujol mull between NaCl windows or in solution using a Specac CaF₂ solution cell. When Fourier transform infrared (FTIR) spectra are discussed, the following abbreviations will be used to indicate the relative absorbance of bands: vs = very strong, s = strong, m = medium, w = weak, vw = very weak, sh = shoulder, br =

broad. Elemental analyses were carried out by the University of Sheffield elemental analysis service on a PerkinElmer 2400 CHNS/O series II elemental analyser in an atmosphere of pure oxygen. ^1H and ^{13}C Nuclear magnetic resonance (NMR) spectra were recorded using a 400 MHz Bruker Avance 400 spectrometer; ^{14}N and ^{119}Sn spectra were kindly recorded by Sue Bradshaw on a 500 MHz Bruker Avance 500 spectrometer. ^1H and ^{13}C NMR spectra were calibrated against the residual solvent peak according to ref^[2]. NMR spectra were processed using *Bruker TOPSPIN v3.2*. DSC measurements were performed on a PerkinElmer Pyris 1 Differential Scanning Calorimeter operated under nitrogen flow (20 ml min^{-1}) with a heating rate of $10 \text{ }^\circ\text{C min}^{-1}$. The instrument was calibrated against a pure indium reference (99.999 %) with a sharp transition at $156.60 \text{ }^\circ\text{C}$, with a well-known enthalpy change of 28.45 J g^{-1} . The samples were sealed in PerkinElmer stainless steel high-pressure capsules ($30 \mu\text{L}$ internal volume) with Au-plated Cu seals, which can operate up to $400 \text{ }^\circ\text{C}$, and 150 bar. Thermogravimetric analysis (TGA) was carried out using a Pyris 1 Thermogravimetric Analyser with a heating rate of $10 \text{ }^\circ\text{C min}^{-1}$ under nitrogen flow (20 ml min^{-1}). Onset temperatures (T_{on}), mass losses, enthalpies of fusion (ΔH_{fus}), and decomposition (ΔH_{dec}) were calculated using the data analysis tools within the Pyris 1 software. Single crystal X-ray diffraction (XRD) data collections were performed at 100 K on a Bruker SMART 4000 diffractometer equipped with a CCD area detector and an Oxford Cryosystems Cobra cryocooler. All data were collected using graphite-monochromated Mo $\text{K}_{\alpha 1,2}$ radiation ($\lambda = 0.71073 \text{ \AA}$). Data were collected using Bruker *APEX^[3]* software and integrated using Bruker *SAINT^[4]* absorption correction was applied using Siemens' Area Detector Absorption correction (*SADABS^[5]*) within *APEX2*. All structures were solved using direct methods for the location of heavy atoms using *SHELXS-97* within *SHELXTL-2013* and refined using *SHELXL-2014^[6,7]*. Carbon-bound hydrogen atom positions were calculated and refined using a riding model, whereas those bound to nitrogen were located via a Fourier difference map, and freely refined. Additional twin refinement was carried out for **2** using the twinning tools within *WinGX^[8,9]* which gave a modest improvement in structure quality and reduced $R1$ from 6 % to 4.5 %. Thermal ellipsoid plots of the crystal structures have been produced using *ORTEP-3 for Windows^[10]*. Powder X-ray diffraction data were collected for a sample of $\text{Sn}(\text{N}_3)_2$ carefully loaded into a 0.7 mm borosilicate glass capillary prior to being mounted and aligned on a Bruker-AXS D8 Advance powder diffractometer operating with Ge-monochromated Cu- $\text{K}_{\alpha 1}$ radiation ($\lambda = 1.54056 \text{ \AA}$). Powder patterns were collected and baselined using the Bruker *DIFFRAC.EVA* software suite v3.1.^[11] A Pawley refinement^[12] was implemented to index the powder pattern using the program *TOPAS^[13]*.

2. Single Crystal X-Ray Diffraction Data

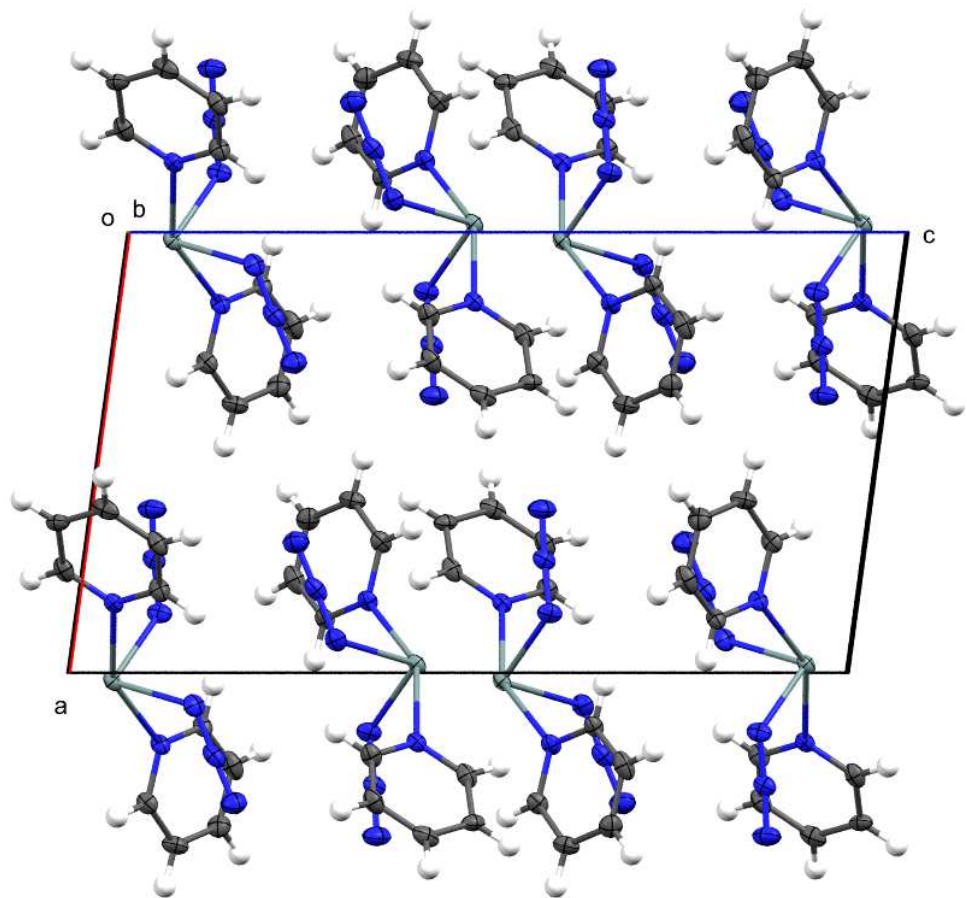


Figure S1. Unit cell of $\text{Sn}(\text{N}_3)_2(\text{py})_2$ (2) viewed along the b -axis, with ellipsoids at the 50 % probability level.

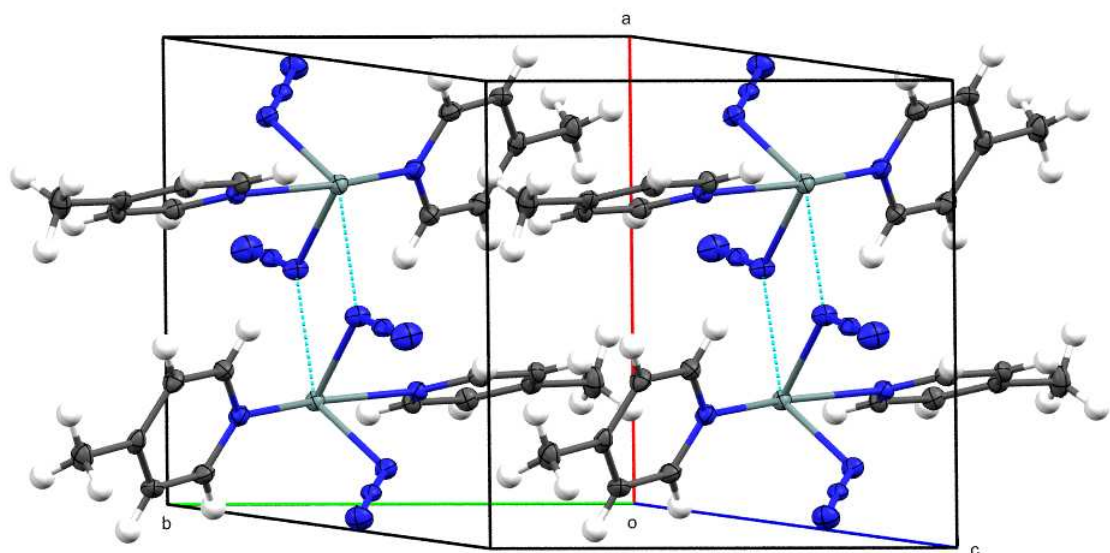


Figure S2. Unit cell packing of $\text{Sn}(\text{N}_3)_2(\text{pic})_2$ (3) showing the ‘dimeric’ interaction between two neighbouring $\text{Sn}-\text{N}_a$ units.

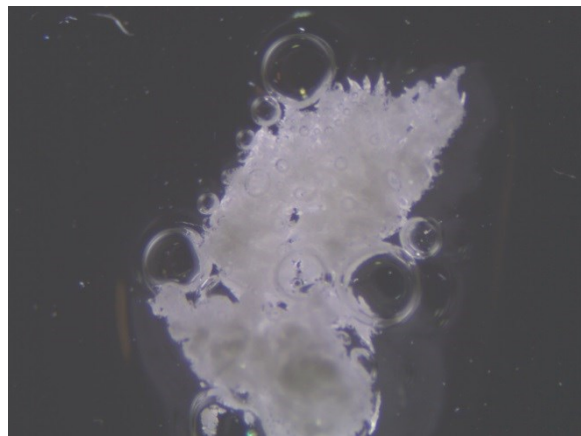


Figure S3. Still image captured of guanidinium triazidostannate (**4**) crystals under a microscope showing evolution of HN_3 caused by moisture in the nujol.

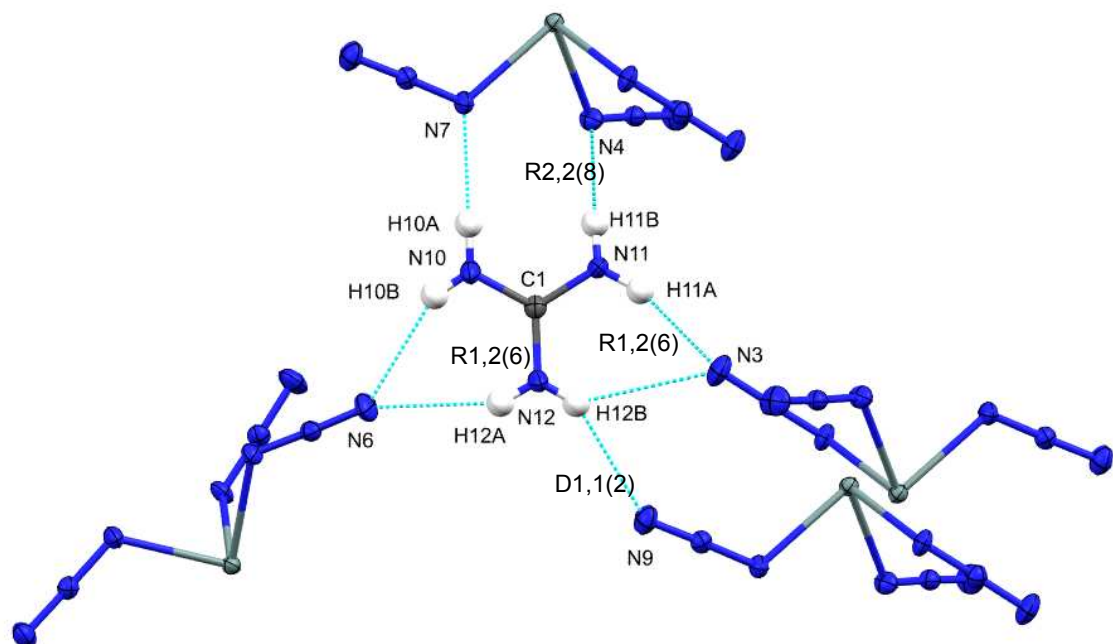


Figure S4. ORTEP diagram showing the graph sets assigned to hydrogen bonds in the structure of guanidinium triazidostannate (**4**).

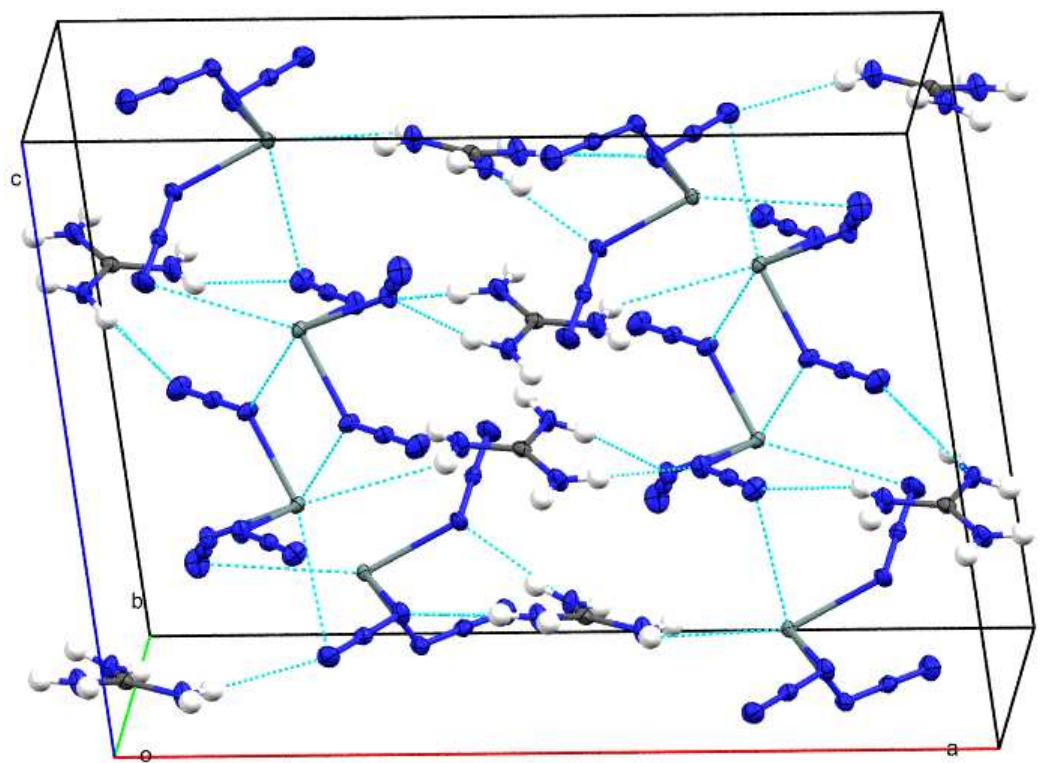


Figure S5. Thermal ellipsoid drawing (50 % probability level) of the unit cell content and intermolecular contacts shorter than the sum of the vdW radii in the crystal of compound **4** at 100 K. H atoms are drawn with a radius of 0.2 Å.

Table S1. Hydrogen bond geometries in the crystal structure of guanidinium triazidostannate (**4**) at 100 K.

#	D–H	A	D–H [Å]	$d(\text{H} \cdots \text{A})$ [Å]	$\angle \text{DHA}$ [°]	$d(\text{D} \cdots \text{A})$ [Å]
1	N10–H10A	N7 ⁱⁱ	0.86	2.180	177	3.040
2	N10–H10B	N6 ^{iv}	0.76	2.391	152	3.089
3	N11–H11A	N3 ⁱ	0.86	2.181	157	2.991
4	N11–H11B	N4 ⁱⁱ	0.84	2.143	168	2.961
5	N12–H12A	N6 ^{iv}	0.78	2.466	148	3.152
6	N12–H12B	N3 ⁱ	0.88	2.753	129	3.321
7	N12–H12B	N9 ⁱⁱⁱ	0.81	2.599	150	3.315

Symmetry codes: *i*) $[x, -y, z+1/2]$, *ii*) $[-x+1, y, -z+3/2]$, *iii*) $[-x+1/2, y-1/2, -z+3/2]$, *iv*) $[x, y+1, z]$

Table S2. Second level graph set matrix for the hydrogen bond network in guanidinium triazidostannate (**4**).

#	1	2	3	4	5	6	7
1	D						
2	C2,2(8)	D					
3	R4,4(20)	C2,2(12)	D				
4	R2,2(8)	C2,2(8)	R4,4(16)	D			
5	C2,2(10)	R1,2(6)	C2,2(12)	C2,2(8)	D		
6	R4,4(20)	C2,2(12)	R1,2(6)	R4,4(20)	C2,2(10)	D	
7	C2,2(8)	C2,2(12)	R4,4(24)	C2,2(10)	C2,2(10)	D2,1(3)	D

2.1 Diazidobis(pyridine)tin (2)

Dataset code	ch1ppx246_0m
Empirical formula	C ₁₀ H ₁₀ N ₈ Sn
Formula weight	360.95
Temperature	100(2) K
Wavelength	0.71073 Å
Crystal system	Monoclinic
Space group	P2 ₁ /c
Unit cell dimensions	$a = 9.9291(4)$ Å $\alpha = 90^\circ$ $b = 7.8096(3)$ Å $\beta = 97.7471(19)$ ° $c = 17.4056(7)$ Å $\gamma = 90^\circ$
Volume	1337.35(9) Å ³
Z	4
Density (calculated)	1.793 g cm ⁻³
Absorption coefficient	1.911 mm ⁻¹
$F(000)$	704
Crystal size	0.27 × 0.13 × 0.10 mm ³
Theta range for data collection	2.070–26.394 °
Index ranges	-12 ≤ h ≤ 12, -9 ≤ k ≤ 9, -21 ≤ l ≤ 21
Reflections collected	13446
Independent reflections	13446 [$R(\text{int}) = ?$]
Completeness to theta = 25.000 °	98.6 %
Absorption correction	Semi-empirical from equivalents
Max. and min. transmission	1.00 and 0.761
Refinement method	Full-matrix least-squares on F^2
Data / restraints / parameters	13446 / 0 / 173
Goodness-of-fit on F^2	1.005
Final R indices [$I > 2\sigma(I)$]	$R1 = 0.0454$, $wR2 = 0.1512$
R indices (all data)	$R1 = 0.0498$, $wR2 = 0.1592$
Extinction coefficient	n/a
Largest diff. peak and hole	1.658 and -2.054 e Å ⁻³

2.2 Diazidobis(4-picoline)tin (3)

Dataset code	ch1ppx257_0m
Empirical formula	C ₁₂ H ₁₄ N ₈ Sn
Formula weight	389.00

Temperature	100(2) K
Wavelength	0.71073 Å
Crystal system	Triclinic
Space group	$P\bar{1}$
Unit cell dimensions	$a = 9.1912(2)$ Å $\alpha = 115.8848(13)$ ° $b = 9.3972(2)$ Å $\beta = 99.0170(13)$ ° $c = 10.0132(2)$ Å $\gamma = 90.6836(13)$ °
Volume	765.32(3) Å ³
Z	2
Density (calculated)	1.688 g cm ⁻³
Absorption coefficient	1.676 mm ⁻¹
$F(000)$	384
Crystal size	0.17 × 0.16 × 0.10 mm ³
Theta range for data collection	3.154–27.554 °
Index ranges	$-11 \leq h \leq 11, -12 \leq k \leq 12, -12 \leq l \leq 13$
Reflections collected	16634
Independent reflections	3503 [$R(\text{int}) = 0.0349$]
Completeness to theta = 25.242 °	99.8 %
Absorption correction	Semi-empirical from equivalents
Max. and min. transmission	1 and 0.854
Refinement method	Full-matrix least-squares on F^2
Data / restraints / parameters	3503 / 0 / 192
Goodness-of-fit on F^2	1.030
Final R indices [$I > 2\sigma(I)$]	$R_1 = 0.0202, wR_2 = 0.0402$
R indices (all data)	$R_1 = 0.0238, wR_2 = 0.0418$
Extinction coefficient	n/a
Largest diff. peak and hole	0.610 and -0.344 e Å ⁻³

2.3 Guanidinium triazidostannate (4)

Dataset code	ch1ppx280_0m
Empirical formula	CH ₆ N ₁₂ Sn
Formula weight	304.87
Temperature	100(2) K
Wavelength	0.71073 Å
Crystal system	Monoclinic
Space group	$C2/c$

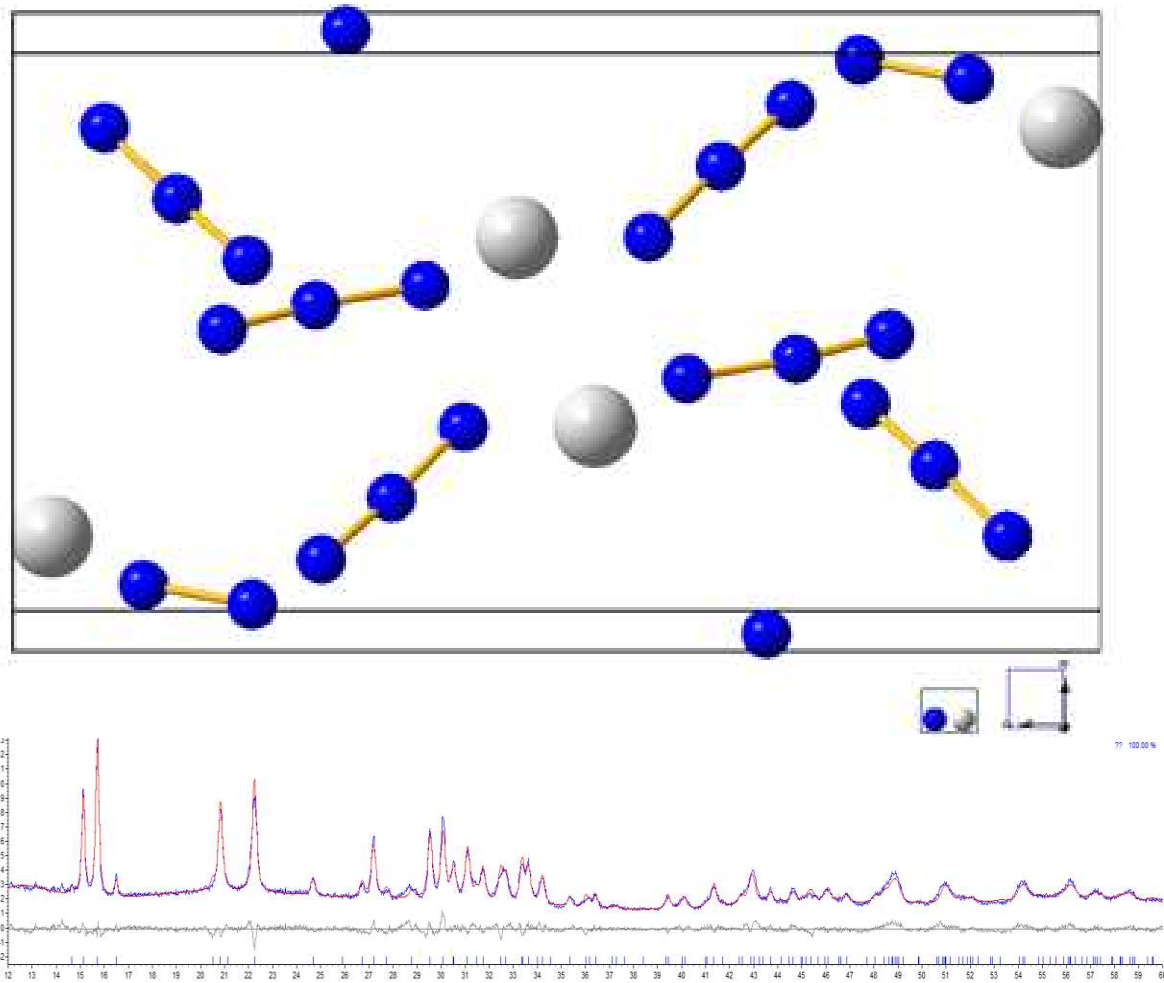
Unit cell dimensions	$a = 18.8171(6)$ Å	$\alpha = 90$ °
	$b = 7.1260(2)$ Å	$\beta = 95.1374(18)$ °
	$c = 13.9984(4)$ Å	$\gamma = 90$ °
Volume	$1869.51(10)$ Å ³	
Z	8	
Density (calculated)	2.166 g cm ⁻³	
Absorption coefficient	2.722 mm ⁻¹	
$F(000)$	1168	
Crystal size	$0.14 \times 0.05 \times 0.05$ mm ³	
Theta range for data collection	2.173–27.508 °	
Index ranges	$-24 \leq h \leq 24, -8 \leq k \leq 9, -18 \leq l \leq 17$	
Reflections collected	15303	
Independent reflections	2154 [$R(\text{int}) = 0.0343$]	
Completeness to theta = 25.242 °	100.0 %	
Absorption correction	Semi-empirical from equivalents	
Refinement method	Full-matrix least-squares on F^2	
Data / restraints / parameters	2154 / 0 / 151	
Goodness-of-fit on F^2	0.985	
Final R indices [$I > 2\text{sigma}(I)$]	$R1 = 0.0180, wR2 = 0.0393$	
R indices (all data)	$R1 = 0.0235, wR2 = 0.0418$	
Extinction coefficient	n/a	
Largest diff. peak and hole	0.395 and -0.309 e Å ⁻³	

3. Powder Diffraction Data

Powder X-ray diffraction data were collected for a sample of Sn(N₃)₂ carefully loaded into a 0.7 mm borosilicate glass capillary prior to being mounted and aligned on a Bruker-AXS D8 Advance powder diffractometer operating with Ge-monochromated Cu-K_{α1} radiation ($\lambda = 1.54056$ Å). Powder patterns were collected and baselined using the Bruker *DIFFRAC.EVA* software suite v3.1.^[11]

Table S3. Atomic positions in the structure of Sn(N₃)₂ (**1**) determined by PXRD, expressed as fractional coordinates.

Atom	Wyck.	x / a	y / b	z / c
Sn1	4e	0.67629	0.53592	0.76861
N1	4e	0.04964	0.87948	0.09580
N2	4e	0.02171	0.77909	0.16447
N3	4e	-0.01484	0.69325	0.22349
N4	4e	0.13858	0.71575	0.76908
N5	4e	0.23506	0.65155	0.67746
N6	4e	0.34748	0.58486	0.58950



$$R_{\text{wp}} = 6.751, R_{\text{exp}} = 3.708, R_{\text{p}} = 5.342, \text{GOF} = 1.820$$

Figure S6. (Top) 3D representation of the structure solution of $\text{Sn}(\text{N}_3)_2$ (**1**) determined by Rietveld refinement; (bottom) Overlay of the predicted vs. observed powder pattern with the subtraction result shown below.

Table S4. Comparison of the geometries in the structures determined from DFT-D calculations compared to those derived from the Rietveld refinement of the PXRD data.

Atom1-Atom2	Distances	
	Theory	Refinement
N1(alpha)-N2(beta)	1.2192	1.2636
N2(beta)-N3(gamma)	1.1657	1.0977
N1(alpha)-N3(gamma)	2.3849	2.3597
N4(gamma)-N5(beta)	1.1688	1.1447
N5(beta)-N6(alpha)	1.2106	1.2146
N4(gamma)-N6(alpha)	2.3794	2.3580
Sn-N1(alpha)	2.3310	2.4188
Sn-N6(alpha)	2.3125	2.3788
Atom1-Atom2-Atom3	Angle	
	Theory	Refinement
N1-N2-N3	179.054	175.791
N4-N5-N6	179.505	176.029

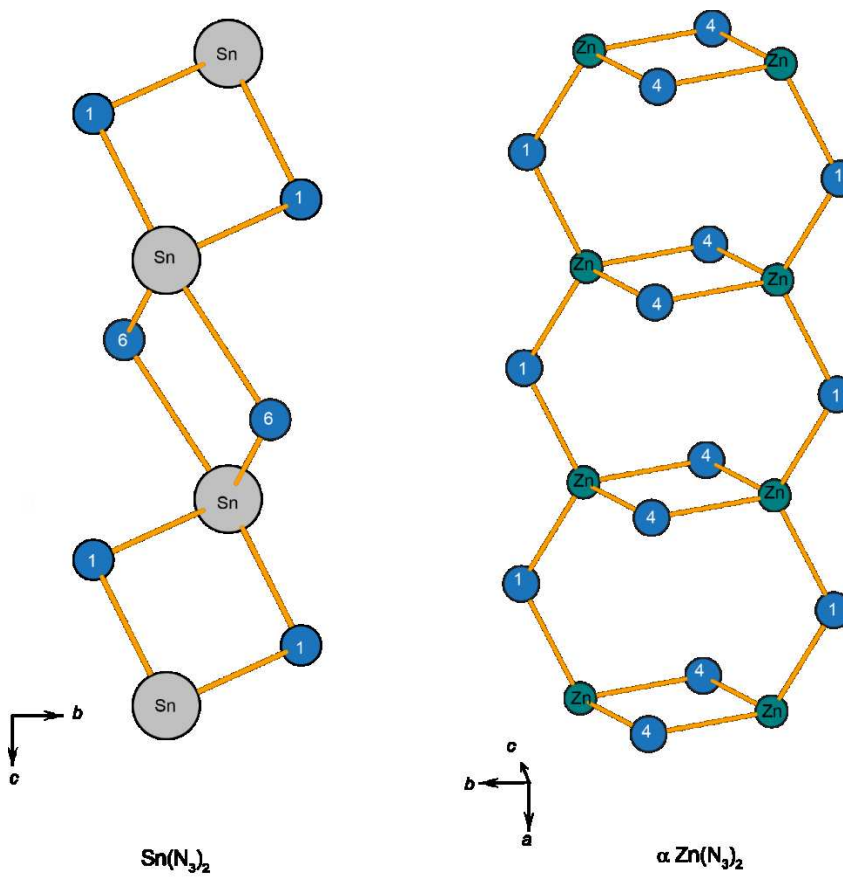


Figure S7. Comparison with $\alpha\text{-Zn}(\text{N}_3)_2$. Left: coordination polymer chain in $\text{Sn}(\text{N}_3)_2$ (1) showing Sn, the bridging N_3 atoms (1) and (6) and the disphenoidal coordination geometry; right: chains formed by both edge- and corner sharing ZnN_4 tetrahedra of $\alpha\text{-Zn}(\text{N}_3)_2$; (1) and (4) denote bridging N_3 atoms.

4. Summary of crystal structure refinement parameters for tin(II) azides 1–4

Table S5. Summary of crystal structure refinement parameters for tin(II) azides 1–4. The structure solution of **1** was obtained from powder x-ray diffraction (PXRD) data. All other structures were determined by single crystal XRD.

	$\text{Sn}(\text{N}_3)_2(\text{py})_2$ (2)	$\text{Sn}(\text{N}_3)_2(\text{pic})_2$ (3)	$\text{C}(\text{NH}_2)_3[\text{Sn}(\text{N}_3)_3]$ (4)	$\text{Sn}(\text{N}_3)_2$ (1)^e
Empirical formula	$\text{C}_{10}\text{H}_{10}\text{N}_8\text{Sn}$	$\text{C}_{12}\text{H}_{14}\text{N}_8\text{Sn}$	$\text{CH}_6\text{N}_{12}\text{Sn}$	N_6Sn
$M / (\text{g mol}^{-1})$	360.92	388.98	304.80	202.73
Crystal system	Monoclinic	triclinic	monoclinic	monoclinic
Space group	$P2_1/c$	$P\bar{1}$	$C2/c$	$P2_1/c$

a / Å	9.9291(4)	9.1912(2)	18.8171(6)	6.4463[7]
b / Å	7.8096(3)	9.3972(2)	7.1260(2)	11.702[1]
c / Å	17.4056(7)	10.0132(2)	13.9984(4)	6.0597[6]
α / °	90	115.8848(13)	90	90
β / °	97.7471(19)	99.0170(13)	95.1374(18)	94.239[6]
γ / °	90	90.6836(13)	90	90
V / Å³	1337.35(9)	765.32(3)	1869.51(10)	455.8[1]
Z	4	2	8	4
T / K	100	100	100	298
D_{calc} / (g cm⁻³)	1.793	1.688	2.166	2.945 ^c
μ / mm⁻¹	1.911	1.676	2.722	5.448 ^c
$F(000)$	704	384	1168	N/A
Crystal size / (mm × mm × mm)	0.27 × 0.13 × 0.10	0.17 × 0.16 × 0.10	0.14 × 0.05 × 0.05	N/A
Θ range for data collection / °	2.070–26.394	3.154–27.554	2.173–27.508	N/A
Limiting indices $h; k; l$	-12, 12; -9, 9; -21, 21	-11, 11; -12, 12; -12, 13	-24, 24; -8, 9; -18, 17	N/A
Reflections collected	13446	16634	15303	N/A
Independent refls.	3004	3503	2154	N/A
R_{int}	0.0363 ^e	0.0349	0.0343	N/A
Completeness to Θ / %	98.6 ($\Theta = 25.00$)	99.8 ($\Theta = 25.242$)	100 ($\Theta = 25.242$)	N/A
Refinement method	<i>a,b</i>	<i>a</i>	<i>a</i>	<i>d</i>
Data / restraints / parameters	3004 / 0 / 173	3503 / 0 / 192	2154 / 0 / 151	N/A

GoF F^2	1.005	1.030	0.985	N/A
Final R indices [$\theta > 2I(\sigma)$]	0.0454	0.0402	0.0180	N/A
R indices (all data)	0.0498	0.0418	0.0235	N/A
Largest diff. peak / hole / ($e \text{ \AA}^{-3}$)	1.66 / -2.05	0.61 / -0.34	0.40 / -0.31	N/A
CCDC Deposition No	1529432	1529433	1529434	N/A
^a Full matrix least squares on F^2 ; ^b Refined as a two-component twin using twinning software tools within WinGX, which reduced the residual electron density and improved R_1 from 0.0577 to 0.0454; ^c Values calculated by the IUCr checkCIF tool (http://journals.iucr.org/services/cif/checkcif.html); ^d Unit cell parameters determined by Pawley refinement and structure determined using the Rietveld method; ^e before twin refinement.				

4.1 Ion volumes

Table S6. Unit cell volumes (V) of guanidinium and tetraphenylphosphonium salts.

salt	$V / \text{\AA}^3$	Z	Reference
C(NH ₂) ₃ Cl	929.9(15)	8	D. J. Haas, D. R. Harris H. H. Mills <i>Acta Cryst.</i> 1965 , <i>19</i> , 676
C(NH ₂) ₃ N ₃	2909.9(7)	24	P. Portius, R. Campbell, unpublished results, 2015.
C(NH ₂) ₃ ClO ₄	456.9(2)	3	Z. Pajak, M. Grottel, A. Kozioł <i>J. Chem. Soc. Faraday Trans. 2</i> 1982 , <i>78</i> , 1529
{C(NH ₂) ₃ } ₃ VF ₆	2800.2(18)	8	C. Black, P. Lightfoot, publCIF
C(NH ₂) ₃ BF ₄	411.6(8)	3	M. Szafraniński <i>CrystEngComm</i> , 2014 , <i>16</i> , 6250
C(NH ₂) ₃ PF ₆	338.2(2)	2	M. Grottel, A. Kozak, A. E. Kozioł, Z. Pajak <i>J. Phys.: Condens. Matter</i> 1989 , <i>1</i> , 7069
C(NH ₂) ₃ Sn(N ₃) ₃	1869.5(1)	8	this paper
PPh ₄ Cl	1964.7(2)	4	J. F. Richardson, J. M. Ball, P. M. Boorman <i>Acta Cryst.</i> 1986 , <i>C42</i> , 1271
PPh ₄ Br	996.6(3)	2	N. W. Alcock, M. Pennington, G. R. Willey <i>Acta Cryst.</i> 1985 , <i>C41</i> , 1549
PPh ₄ I	1001.7(2)	2	E. E. Schweizer, C. J. Baldacchini, A. L. Rheingold <i>Acta Cryst.</i> 1989 , <i>C45</i> , 1236
PPh ₄ NCO	955.3(1)	2	A. Bernsdorf, M. Köckerling <i>Z. Kristallogr. NCS</i> 2012 , <i>227</i> , 85
PPh ₄ PF ₆	1068.9(8)	2	H. J. Banbery, T. A. Hamor <i>Acta Cryst.</i> 1988 , <i>C44</i> , 1683
PPh ₄ ClO ₄	3998.2(2)	8	S. R. Batten, A. R. Harris, K. S. Murray, Keith S. <i>Acta Crystallogr. Section C</i> 2000 , <i>56</i> , 11 1394
PPh ₄ N ₃	987.6(4)	2	R. Haiges, T. Schroer, M. Yousufuddin, K. O. Christe <i>Z. Anorg. Allg. Chem.</i> 2005 , <i>631</i> , 2691
PPh ₄ Sn(N ₃) ₃	1222.1(1)	2	B. Peerless, T. Keane, A. J. H. M. Meijer, P. Portius <i>Chem. Commun.</i> 2015 , <i>51</i> 7407

Using the anion radii published by H. D. B. Jenkins, H. K. Roobottom, J. Passmore and L. Glasser, *Inorg. Chem.* **1999**, *38*, 3609, the average volumes for tetraphenylphosphonium and guanidinium cations were calculated based on six or seven reference crystal structures each (see table above):

$V(\text{PPh}_4)^+ = 431(\pm 10) \text{ \AA}^3$, $V(\text{C}(\text{NH}_2)_3^+) = 68(\pm 7) \text{ \AA}^3$. These values were subtracted from the molar volumes of the triazidostannate salts, resulting in the apparent volume of the $\text{Sn}(\text{N}_3)_3^-$ ion of $180(\pm 10) \text{ \AA}^3$ in $\text{PPh}_4\text{Sn}(\text{N}_3)_3$ and $166(\pm 7) \text{ \AA}^3$ in $\text{C}(\text{NH}_2)_3\text{Sn}(\text{N}_3)_3$. A direct comparison of the crystal structures of $\text{PPh}_4\text{Sn}(\text{N}_3)_3$, PPh_4N_3 , $\text{C}(\text{NH}_2)_3\text{Sn}(\text{N}_3)_3$ and $\text{C}(\text{NH}_2)_3\text{N}_3$ also points to the $\text{Sn}(\text{N}_3)_3^-$ ion occupying less volume in the guanidinium salt ($-4.8(\pm 0.3) \text{ \AA}^3$).

5. Density Functional Theory Calculations

Structure optimizations were performed using density functional theory plus dispersion (DFT-D) and the plane-wave pseudopotential method as implemented in *CASTEP* version 16.1,^[14] utilizing the dispersion correction scheme of Tkatchenko & Scheffler.^[15] Treatment of electronic exchange and correlation was handled by the generalized gradient approximation (GGA) formalized by Perdew, Burke and Ernzerhof (PBE), the density mixing scheme of Pulay was implemented with mixing amplitude, maximum g-vector, number of extra bands, smearing scheme and smearing width of 0.5, 1.5 \AA^{-1} , 14, Gaussian and 0.1 eV, respectively.^[16] On-the-fly (OTF)^[17] pseudopotentials generated using the *CASTEP* code were used; the plane-wave cutoff energy used throughout was 950 eV, which ensured convergence of both lattice parameters and total energies (to less than 0.002 meV per atom). Brouillon zone sampling was obtained using a Monkhorst-Pack^[18] grid of $3 \times 2 \times 4$ (spacing $< 0.5 \text{ \AA}^{-1}$, 5 k-points). The structures were relaxed [using the Broyden, Fletcher, Goldfarb and Shannon (BFGS)^[19] method] to allow both atomic coordinates and unit cell vectors to optimize simultaneously while constraining space group geometry (convergence criteria: maximum change in system energy = 5×10^{-6} eV, maximum root-mean-square (RMS) force = 0.01 eV \AA^{-1} , maximum RMS stress = 0.01 GPa and maximum RMS displacement = $5 \times 10^{-4} \text{ \AA}$).

6. Spectroscopic Data

6.1 FTIR Spectra

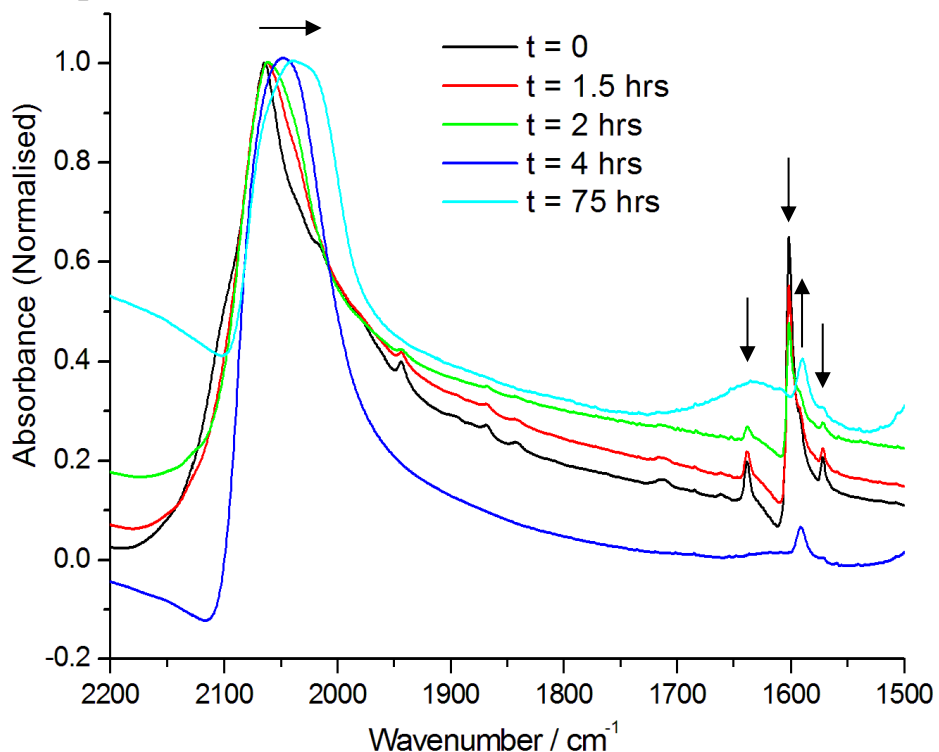


Figure S6. FTIR spectra of crystalline **2** upon exposure to air, with samples taken at the specified time intervals. The spectra are normalized to the $\nu_{as}(N_3)$ peak maximum absorption band to show more clearly the disappearance of coordinated pyridine absorption bands, the shift to lower energy of the $\nu_{as}(N_3)$ peak maximum.

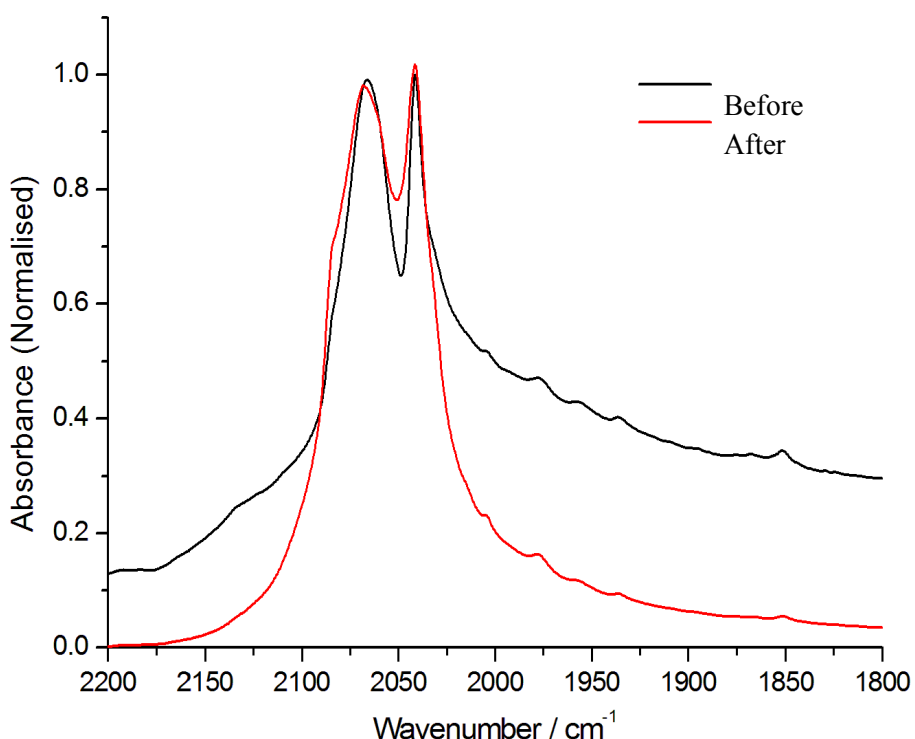


Figure S7. FTIR spectrum of a nujol suspension of $Sn(N_3)_2(pic)_2$ (**3**) before and after exposure to air overnight.

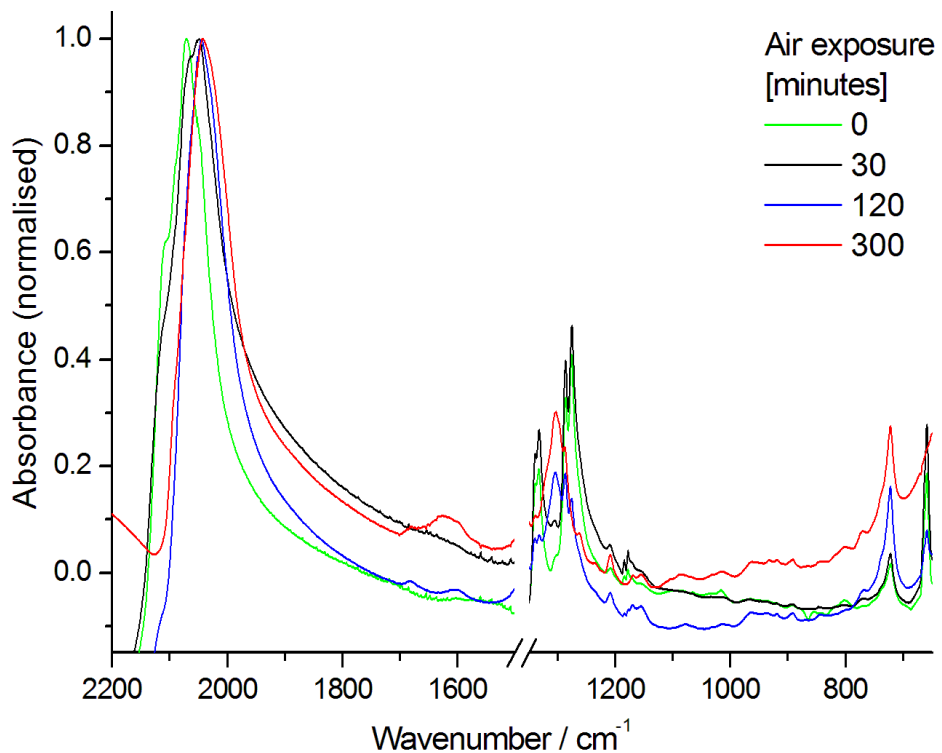


Figure S8. FTIR spectral series showing the effect of exposure of $\text{Sn}(\text{N}_3)_2$ (**1**) to air, which causes gradual shift to lower energy. The spectra are normalized to the $\nu_{\text{as}}(\text{N}_3)$ peak maximum.

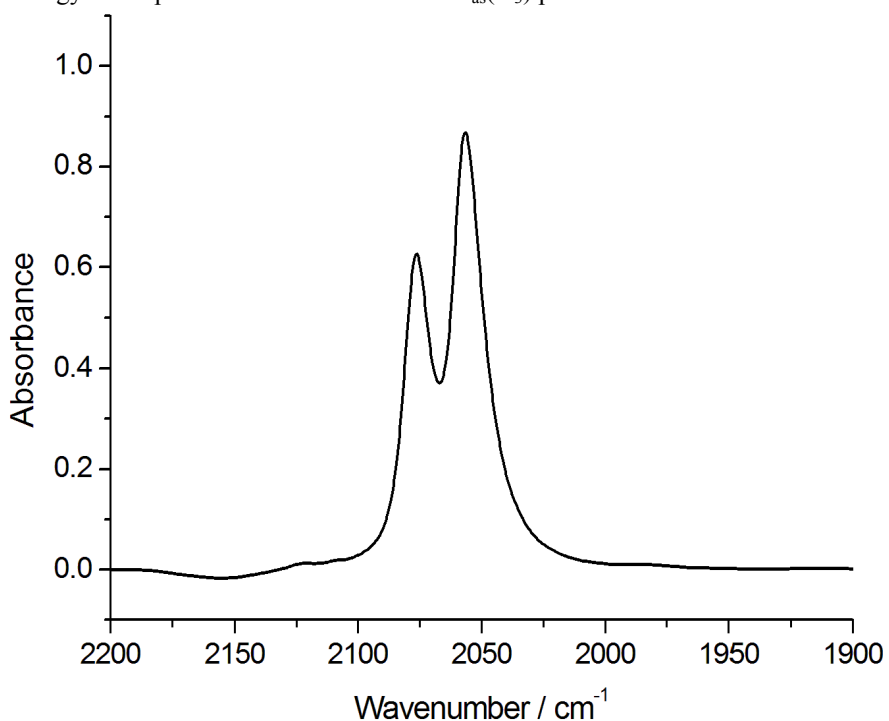


Figure S9. FTIR spectrum of $\text{Sn}(\text{N}_3)_2(\text{py})_2$ (**2**) in pyridine solution showing the asymmetric azide stretch region.

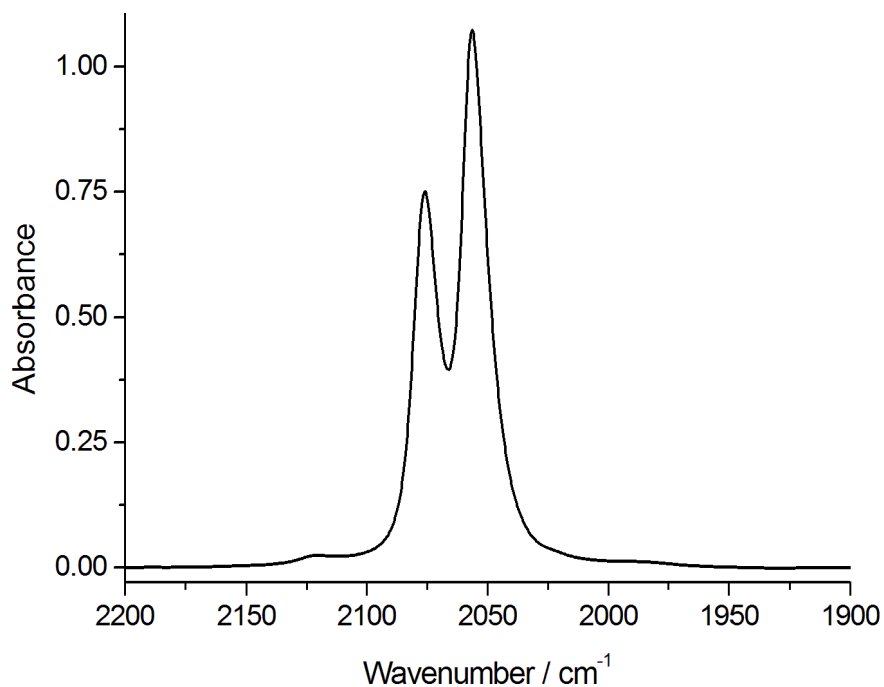


Figure S10. FTIR spectrum of $\text{Sn}(\text{N}_3)_2(\text{pic})_2$ (**3**) in 4-picoline solution showing the asymmetric azide stretch region.

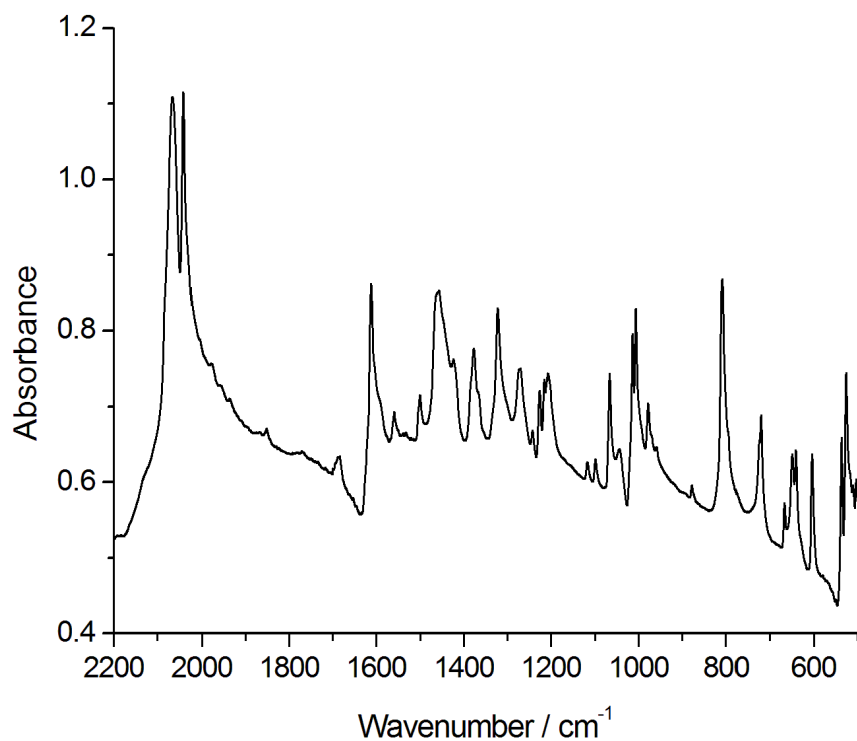


Figure S11. FTIR spectrum of $\text{Sn}(\text{N}_3)_2(\text{pic})_2$ (**3**) as a nujol suspension.

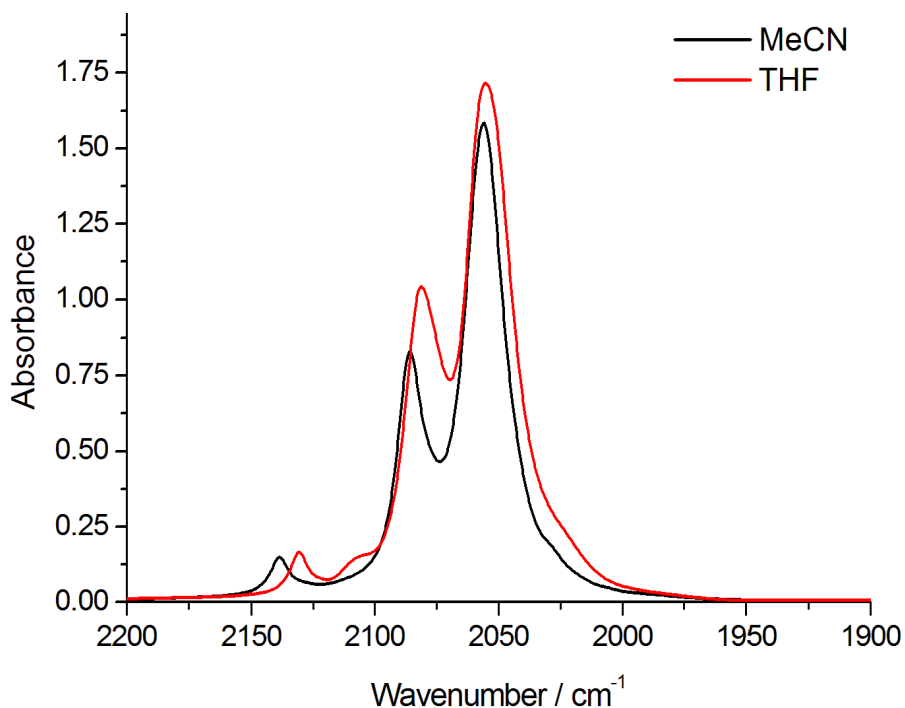


Figure S12. FTIR spectra of guanidinium triazidostannate (**4**) in acetonitrile (black) and THF (red) solutions.

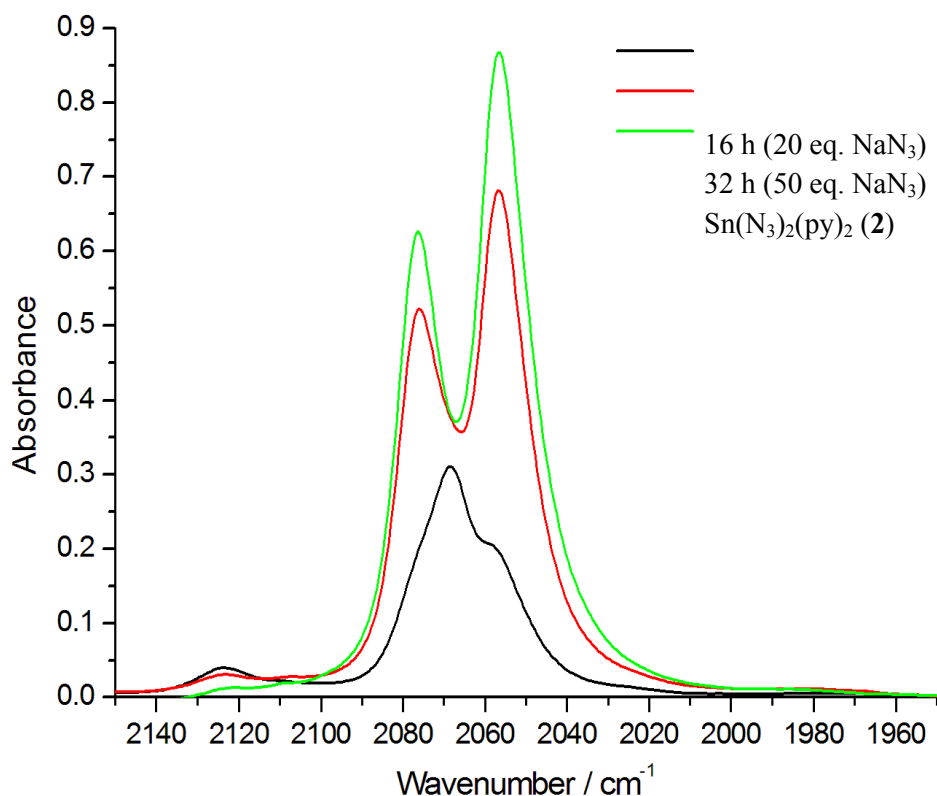


Figure S13. In-situ FTIR spectra from the reaction of SnCl₂ with NaN₃ in pyridine, compared to a reference spectrum of Sn(N₃)₂(py)₂ (**2**). Black: Reaction solution after reaction of SnCl₂ with NaN₃ (20 equiv.); red: after reaction with second batch of NaN₃ (30 equiv.); green: reference spectrum of Sn(N₃)₂(py)₂ (**2**) in pyridine prepared by *via* SnF₂; N.B.: a small peak is visible at 2123 cm⁻¹ due to HN₃.

6.2 NMR Spectra

$\text{Sn}(\text{N}_3)_2(\text{py})_2$ in d_5 -pyridine

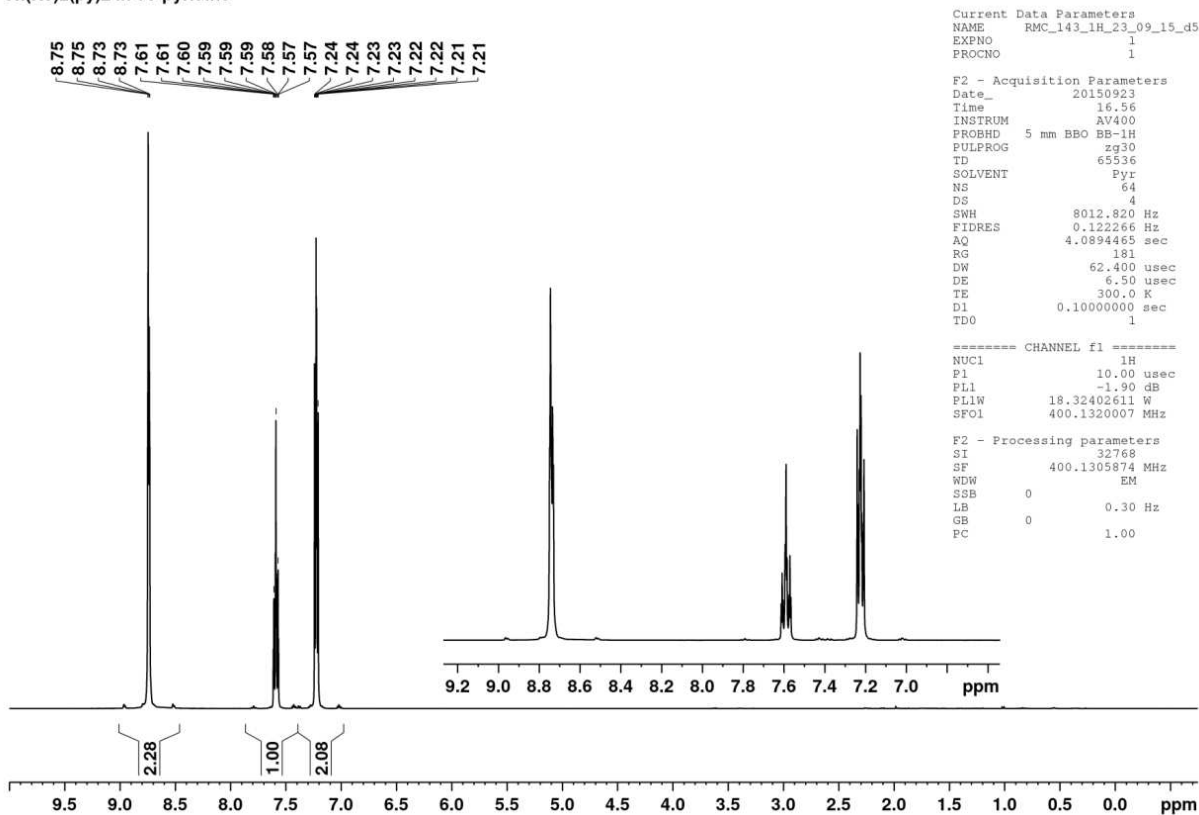


Figure S14. ^1H NMR of $\text{Sn}(\text{N}_3)_2(\text{py})_2$ (**2**) in d_5 -pyridine. The spectrum has been calibrated against the solvent residual according to Cambridge Isotope Laboratories: http://www2.chem.umd.edu/nmr/reference/isotope_solvent.pdf. Analysis of the splitting patterns observed in the multiplets seem to be similar to those of h_5 -pyridine.^[20] See Figure S15 below for an expanded view showing the coupling with ^{13}C .

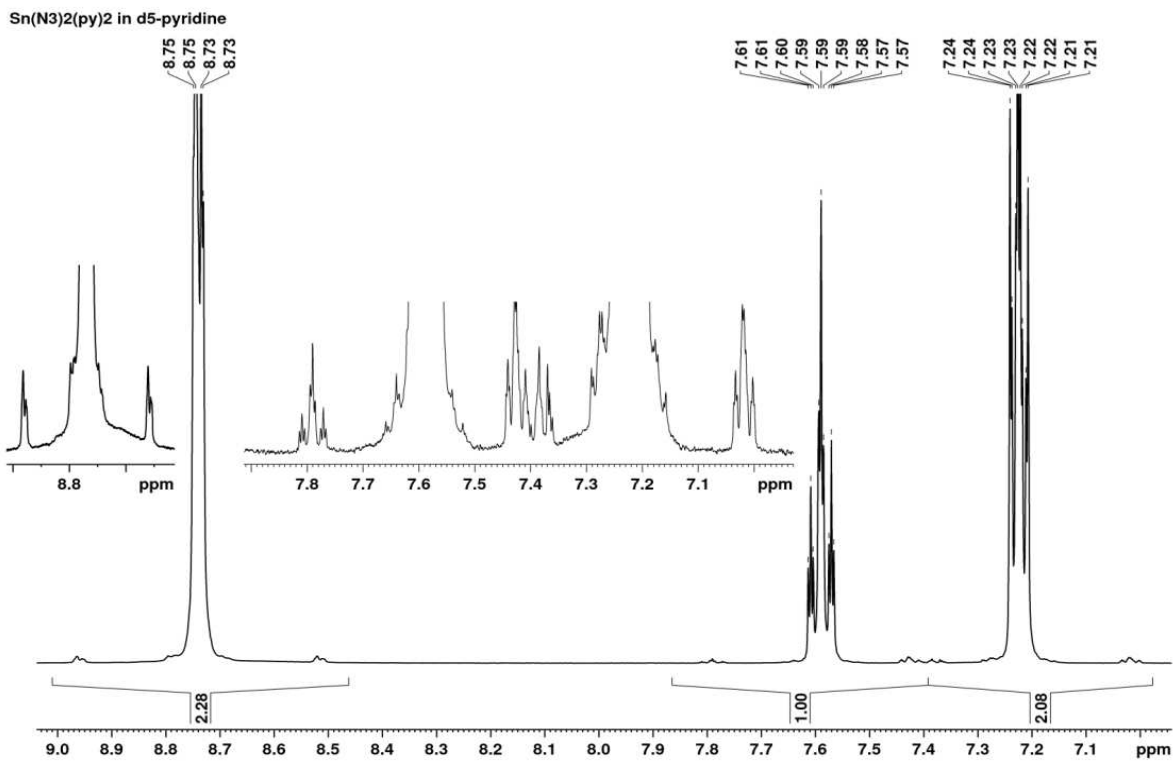


Figure S15. Expanded view of the ¹H NMR spectrum of Sn(N₃)₂(py)₂ (**2**) in *d*₅-pyridine showing the fine structure of satellite peaks due to ¹H-¹³C coupling. Spinning side band observed \pm 20 Hz on either side for all protons. Coupling constants: $J(^1\text{H}_{\text{ortho}}\text{-}^{13}\text{C}) = 178$ Hz; $J(^1\text{H}_{\text{meta}}\text{-}^{13}\text{C}) = 40$ Hz, $J(^1\text{H}_{\text{meta}}\text{-}^{13}\text{C}) = 162$ Hz; $J(^1\text{H}_{\text{para}}\text{-}^{13}\text{C}) = 40$ Hz, $J(^1\text{H}_{\text{para}}\text{-}^{13}\text{C}) = 163$ Hz.

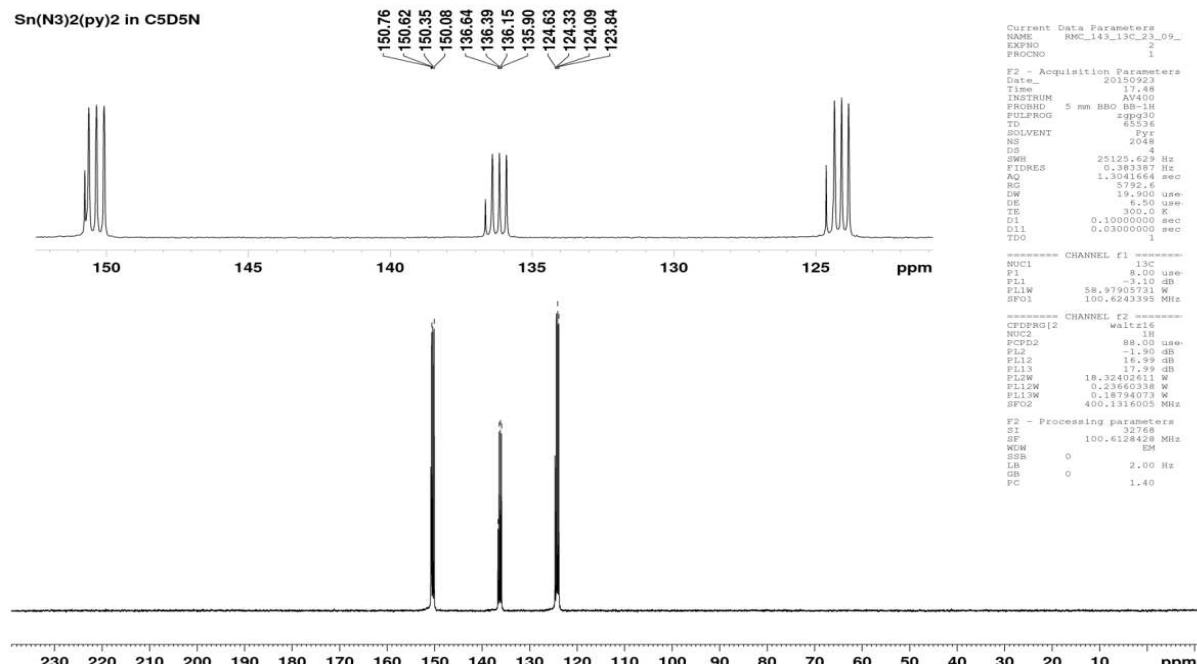


Figure S16. ¹³C NMR spectrum of Sn(N₃)₂(py)₂ (**2**) in *d*₅-pyridine calibrated against the solvent residual peak at 150.35 ppm (1:1:1 triplet) according to Cambridge Isotope Laboratories: http://www2.chem.umd.edu/nmr-reference/isotope_solvent.pdf. Less intense singlet peaks are visible very close to the solvent residual peaks, which are likely to be free pyridine.

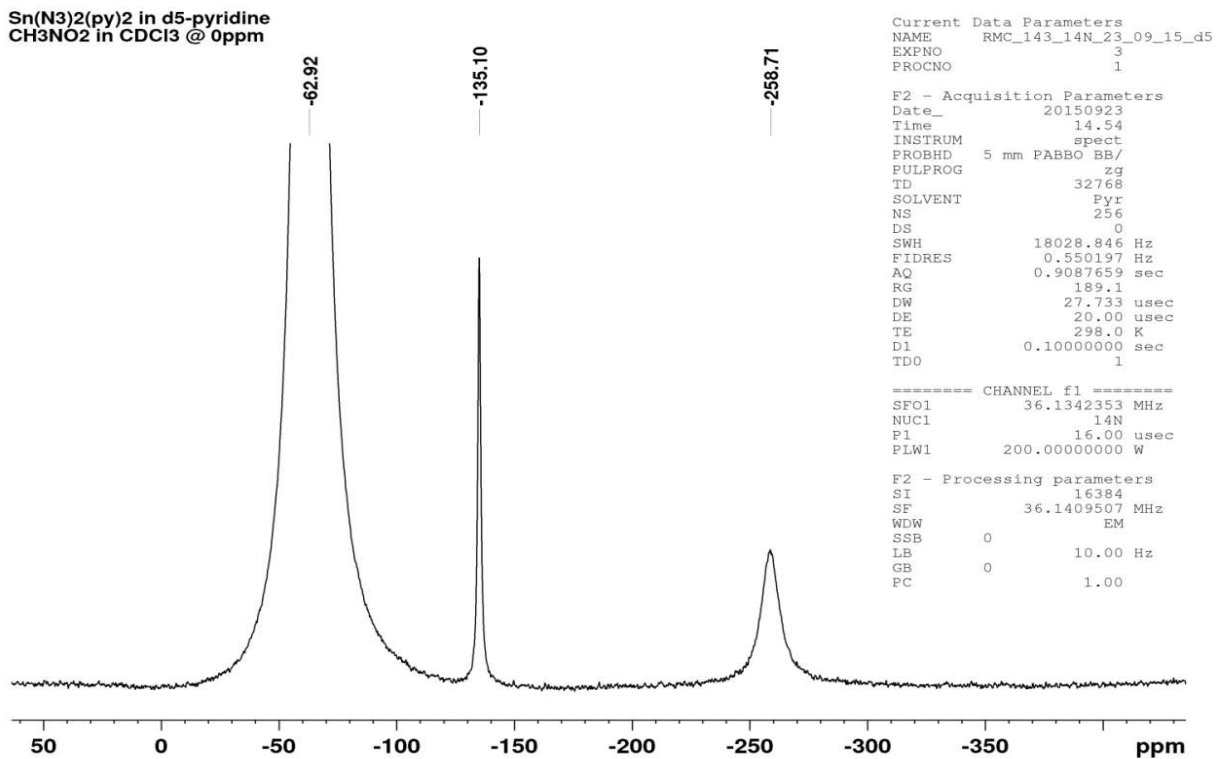


Figure S17. ¹⁴N NMR of Sn(N₃)₂(py)₂ (**2**) in *d*₅-pyridine referenced to CH₃NO₂ in CDCl₃ at 0 ppm.

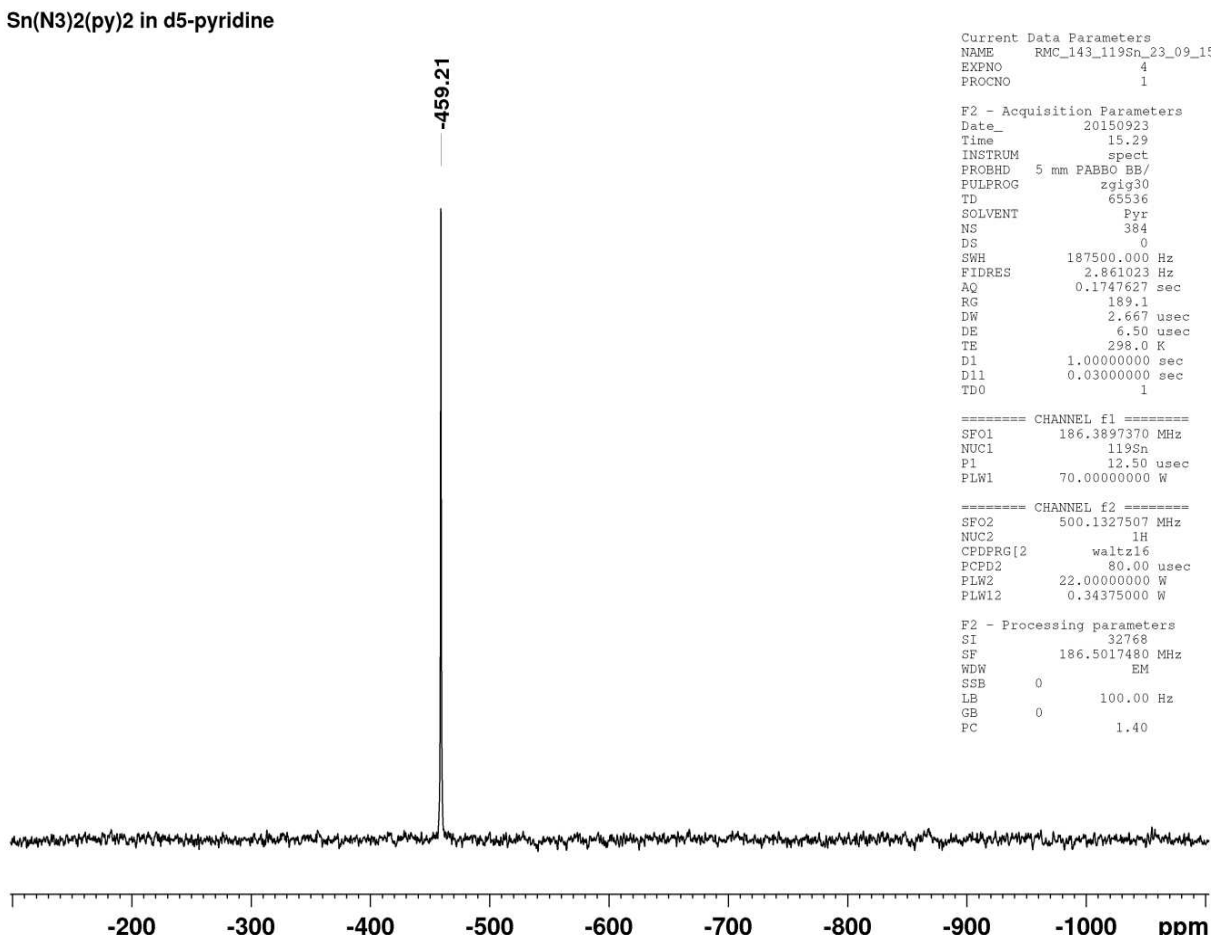


Figure S18. ¹¹⁹Sn NMR of Sn(N₃)₂(py)₂ (**2**) in *d*₅-pyridine.

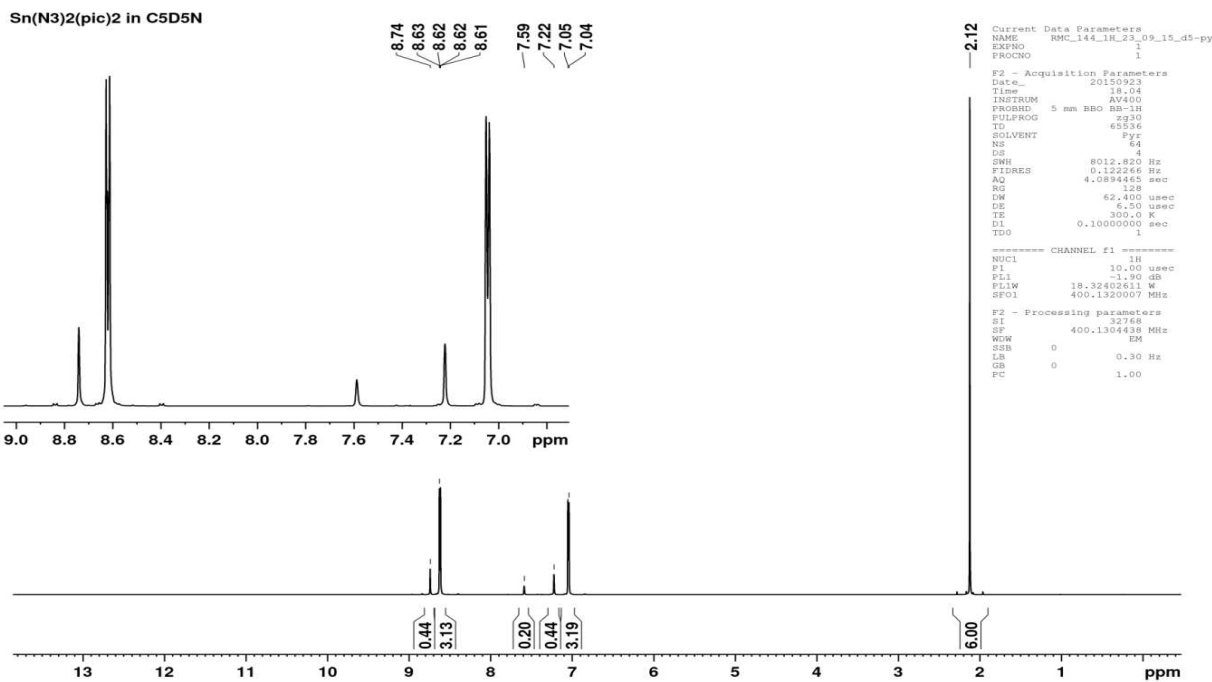


Figure S19. ^1H NMR spectrum of $\text{Sn}(\text{N}_3)_2(\text{pic})_2$ (**3**) in d_5 -pyridine, calibrated against solvent residual at 8.74 ppm according to Cambridge Isotope Laboratories: http://www2.chem.umd.edu/nmr/reference/-isotope_solvent.pdf.

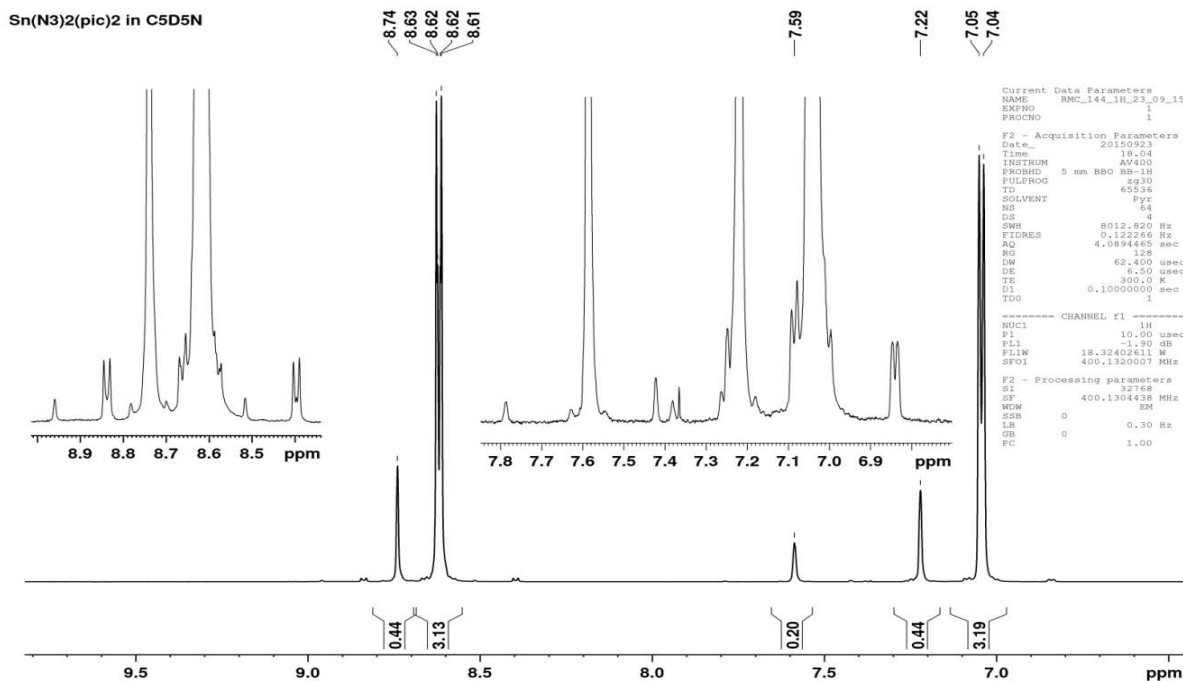


Figure S20. Expanded view of the ^1H NMR spectrum of $\text{Sn}(\text{N}_3)_2(\text{pic})_2$ (**3**) in d_5 -pyridine showing the satellite peaks due to coupling to ^{13}C and ^{119}Sn . Coupling constants for 4-picoline: $J(^1\text{H}_{\text{methyl}}-^{13}\text{C}) = 33 \text{ Hz}$, $J(^1\text{H}_{\text{methyl}}-^{13}\text{C}) = 127 \text{ Hz}$; $J(^1\text{H}_{\text{ortho}}-^{13}\text{C}) = 33 \text{ Hz}$, $J(^1\text{H}_{\text{ortho}}-^{13}\text{C}) = 177 \text{ Hz}$; $J(^1\text{H}_{\text{meta}}-^{13}\text{C}) = 33 \text{ Hz}$, $J(^1\text{H}_{\text{meta}}-^{13}\text{C}) = 160 \text{ Hz}$. Coupling constants for pyridine solvent residual: $J(^1\text{H}_{\text{ortho}}-^{13}\text{C}) = 33 \text{ Hz}$, $J(^1\text{H}_{\text{ortho}}-^{13}\text{C}) = 178 \text{ Hz}$; $J(^1\text{H}_{\text{para}}-^{13}\text{C}) = 33 \text{ Hz}$, $J(^1\text{H}_{\text{para}}-^{13}\text{C}) = 163 \text{ Hz}$; $J(^1\text{H}_{\text{meta}}-^{13}\text{C}) = 33 \text{ Hz}$, $J(^1\text{H}_{\text{meta}}-^{13}\text{C}) = 163 \text{ Hz}$.

Sn(N₃)₂(pic)₂ in d₅-pyridine

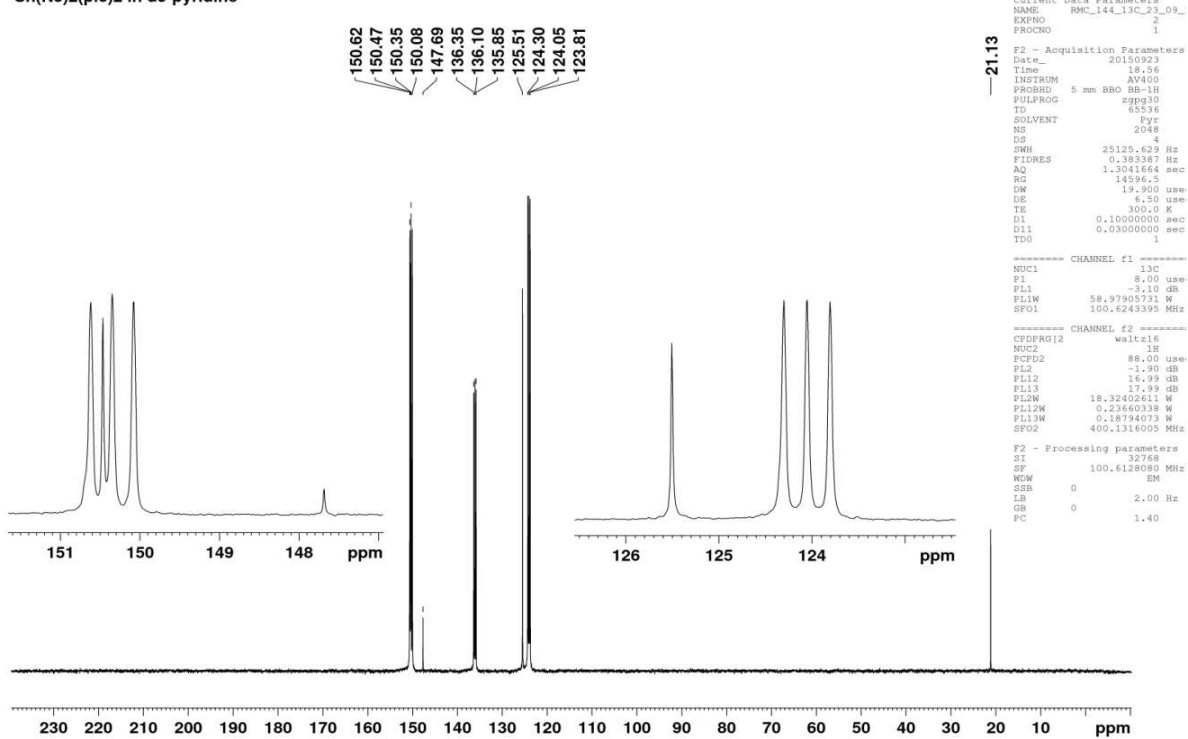


Figure S21. ¹³C NMR spectrum of Sn(N₃)₂(pic)₂ (**3**) in *d*₅-pyridine.

Sn(N₃)₂(pic)₂ in d₅-pyridine
reference CH₃NO₂ in CDCl₃ @ 0ppm

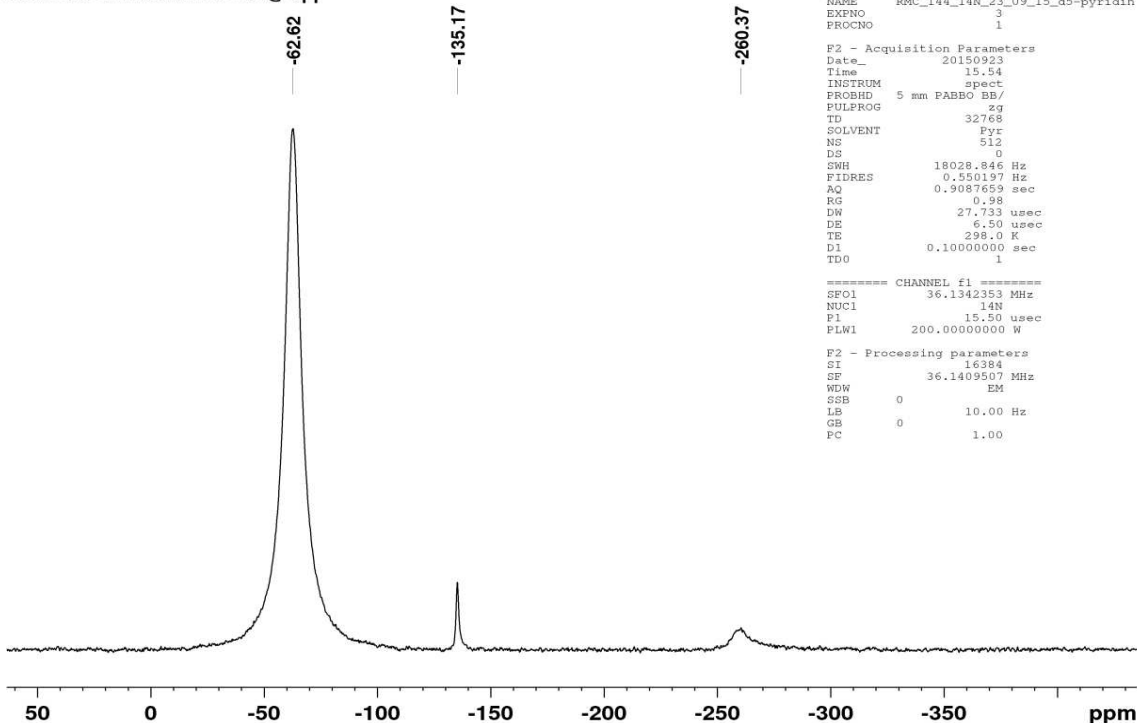


Figure S22. ¹⁴N NMR of Sn(N₃)₂(pic)₂ (**3**) in *d*₅-pyridine referenced against CH₃NO₂ in CDCl₃ at 0 ppm. FWHM: Solvent residual -62.6, 292 Hz; N_β = -135.1, 51 Hz; N_α = -260.4, 305 Hz.

Sn(N₃)₂(pic)₂ in d₅-pyridine

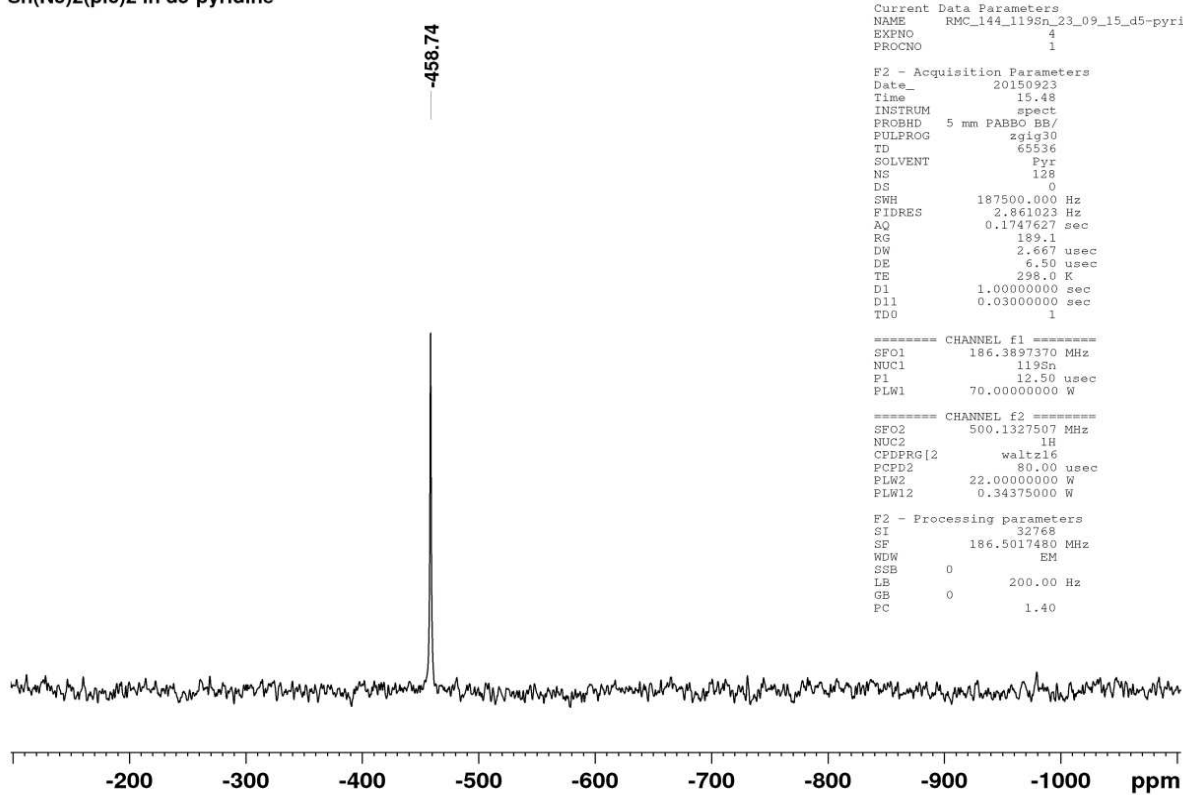


Figure S23. ¹¹⁹Sn NMR of Sn(N₃)₂(pic)₂ (**3**) in *d*₅-pyridine.

Guanidinium Triazidostannate in CD₃CN

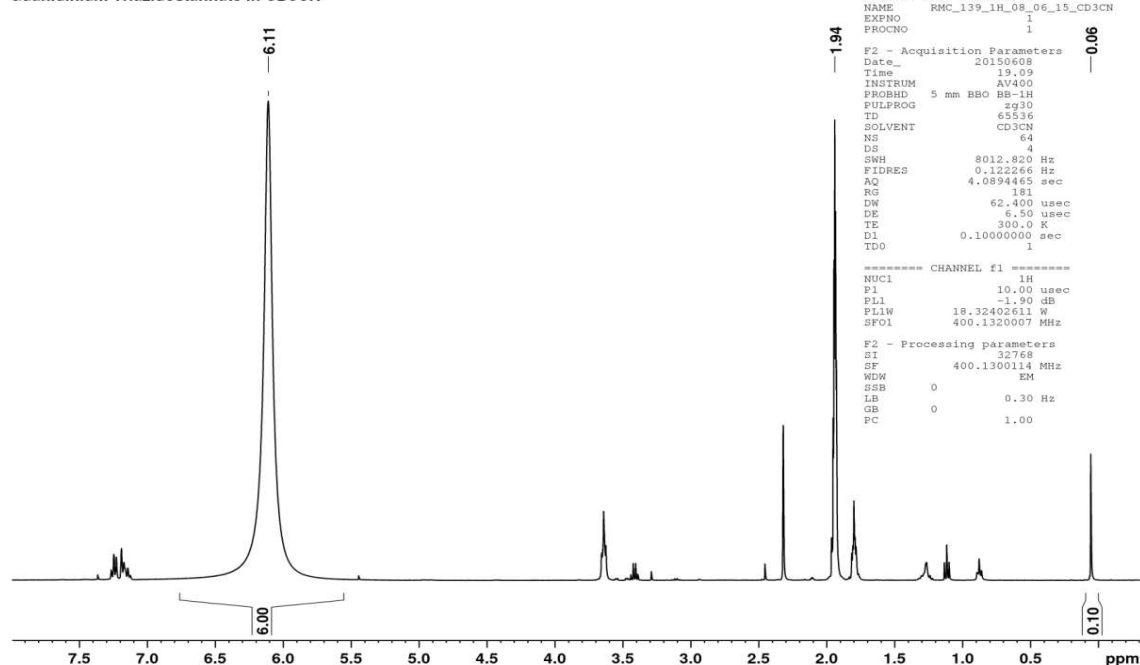


Figure S24. ¹H NMR of guanidinium triazidostannate (**4**) in CD₃CN, with a trace (*ca.* 1 %) of residual TMS-N₃ at 0.05 ppm. Additional peaks are contamination of the NMR solvent by Et₂O, THF, *n*-hexane and toluene.

Guanidinium Triazidostannate in CD₃CN

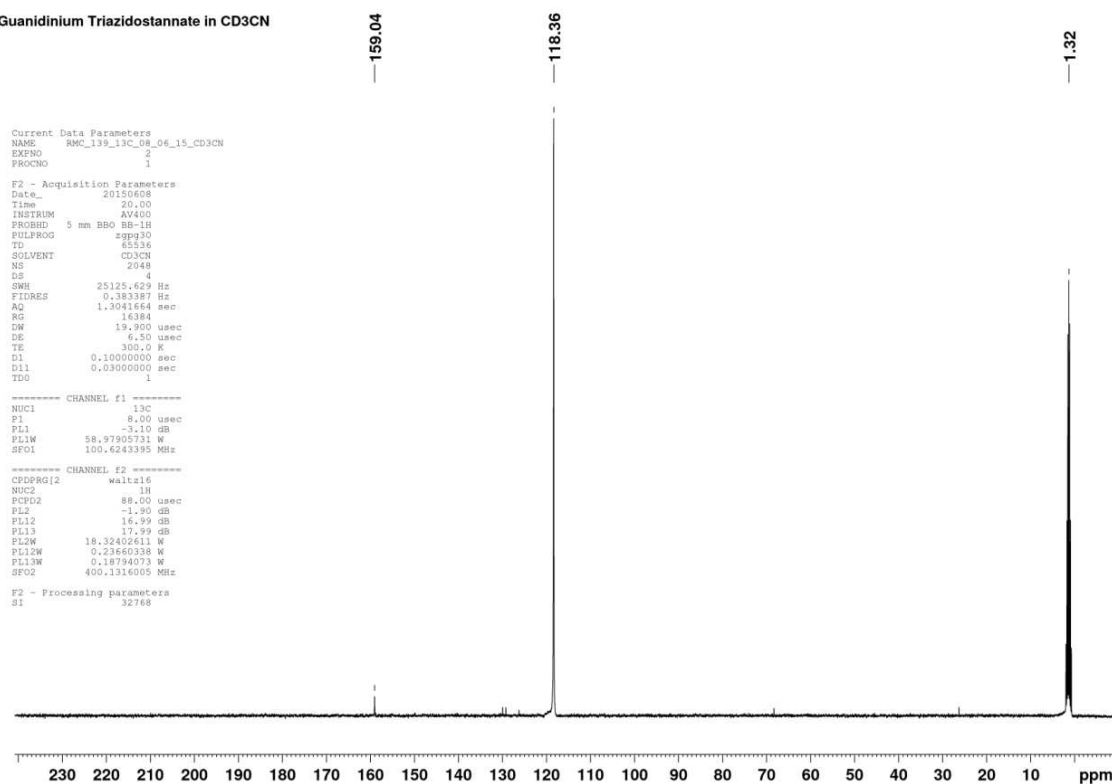


Figure S25. ¹³C NMR (CPD) of guanidinium triazidostannate (**4**) in CD₃CN. Additional peaks are due to contamination of the NMR solvent with toluene and THF.

Guanidinium Triazidostannate in CD₃CN

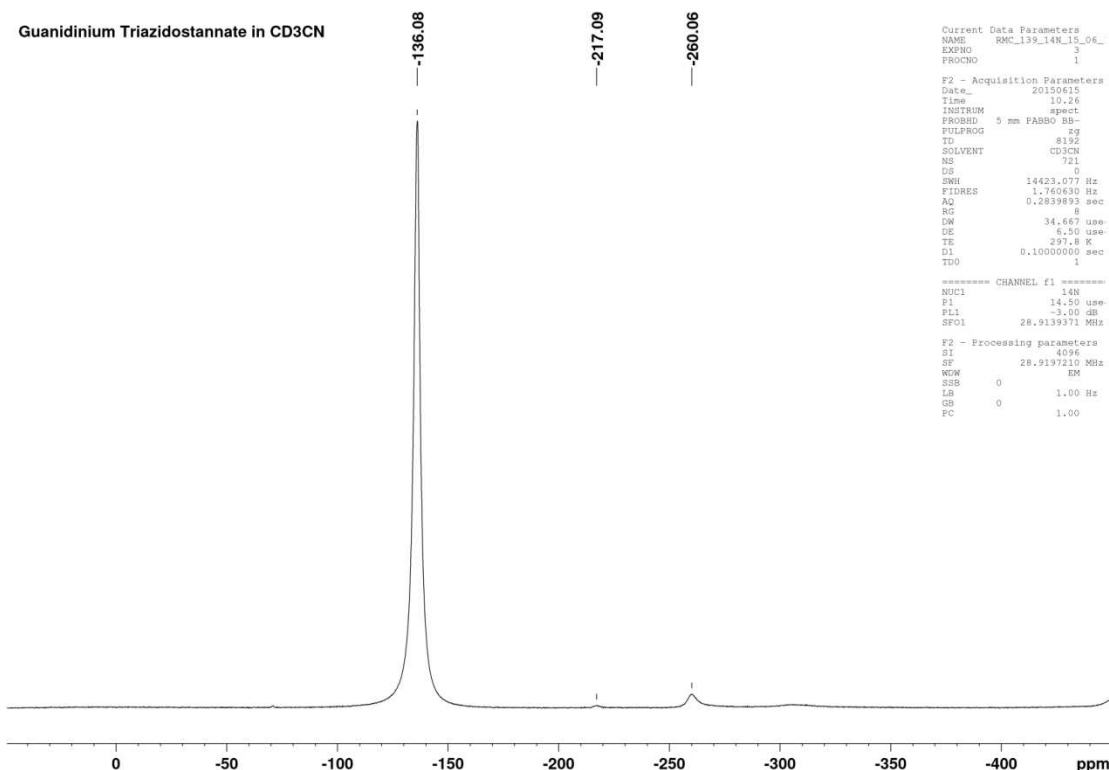


Figure S25. ¹⁴N NMR of guanidinium triazidostannate (**4**) in CD₃CN. δ / ppm = -217.09, $\Delta\nu_{1/2}$ = 108 Hz, -260.06 $\Delta\nu_{1/2}$ = 162 Hz.

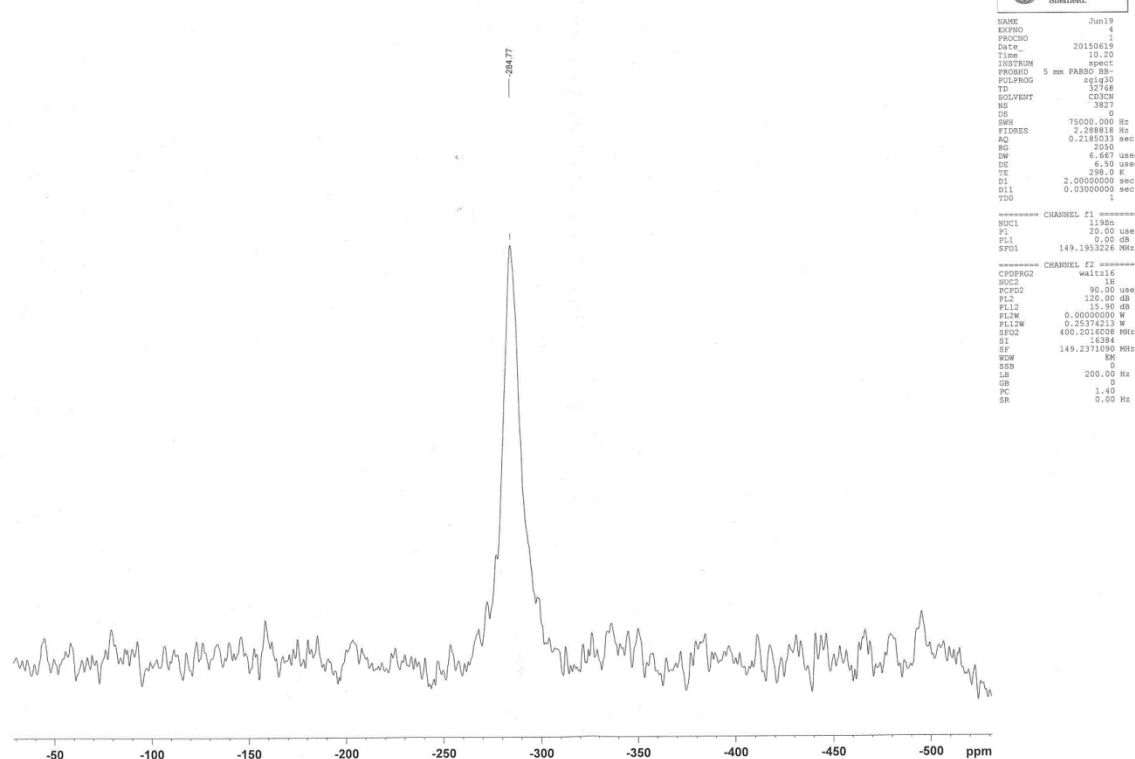


Figure S26. ¹¹⁹Sn NMR of guanidinium triazidostannate (**4**) in CD₃CN. Spectrum shows a single relatively low intensity peak (limited by solubility) at δ / ppm = -284.77.

7. Calorimetric and Thermogravimetric Data

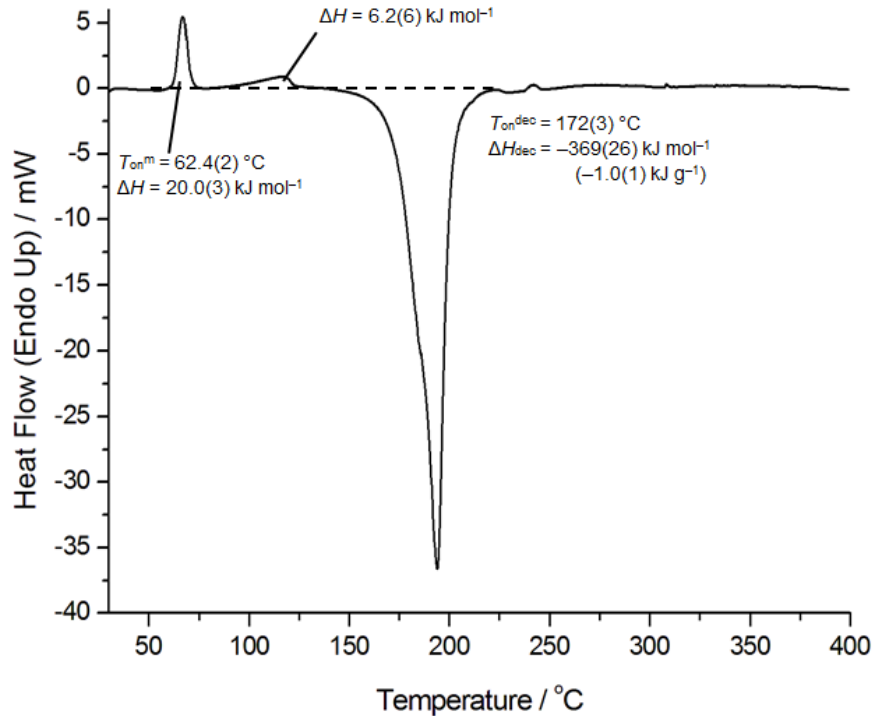


Figure S27. Differential scanning calorimetry trace of diazidobis(pyridine)tin (**2**). Heating rate 10 °C min⁻¹, nitrogen flow rate 20 ml min⁻¹.

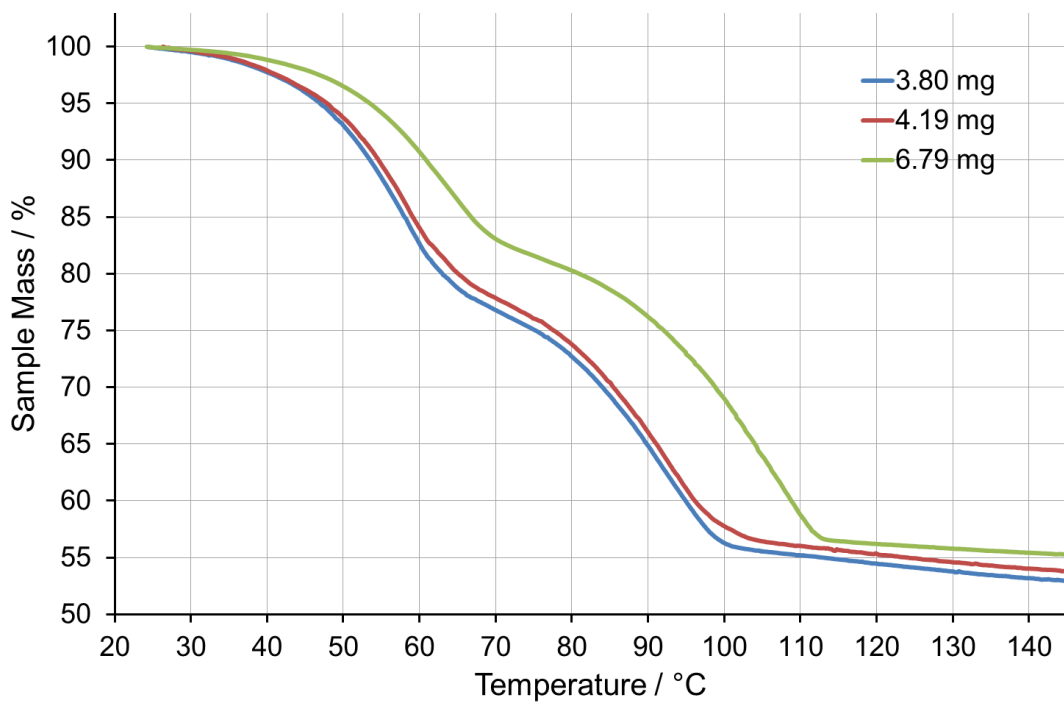


Figure S28. Thermograms (3.80, 4.19 and 6.79 mg) of $\text{Sn}(\text{N}_3)_2(\text{py})_2$ (**2**) showing two mass loss steps for each equivalent of pyridine, leaving behind $\text{Sn}(\text{N}_3)_2$ (**1**). Heating rate $10\text{ }^\circ\text{C min}^{-1}$, nitrogen flow rate 20 ml min^{-1} .

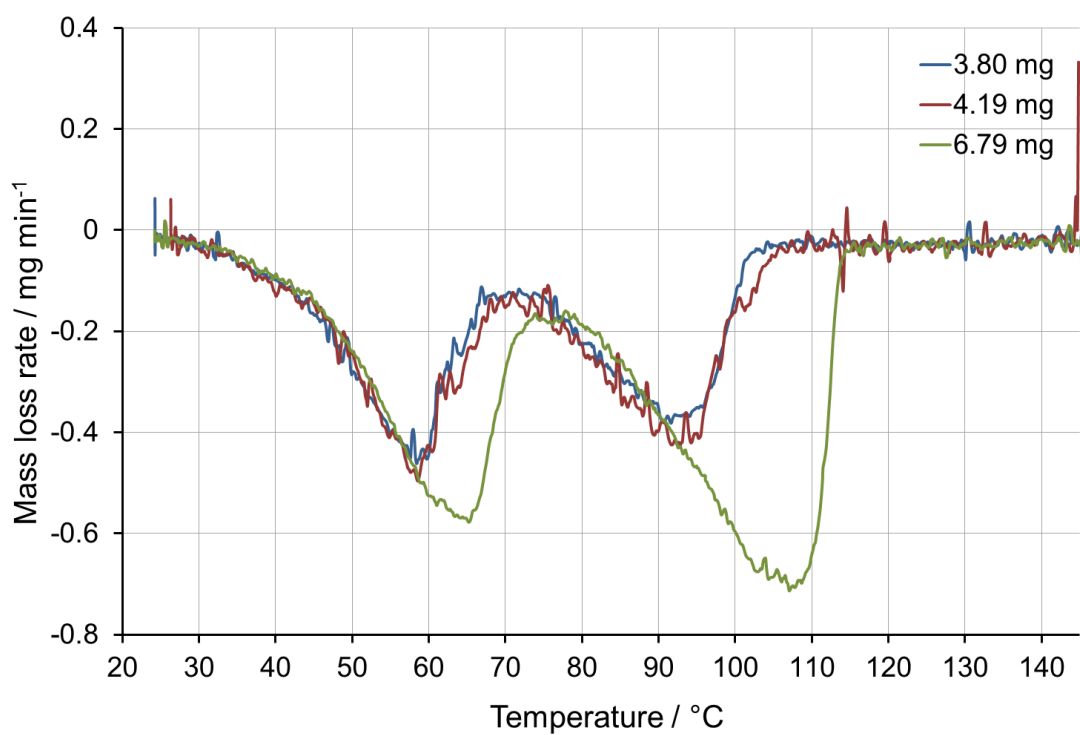


Figure S29. Differential thermograms derived from Fig. S28.

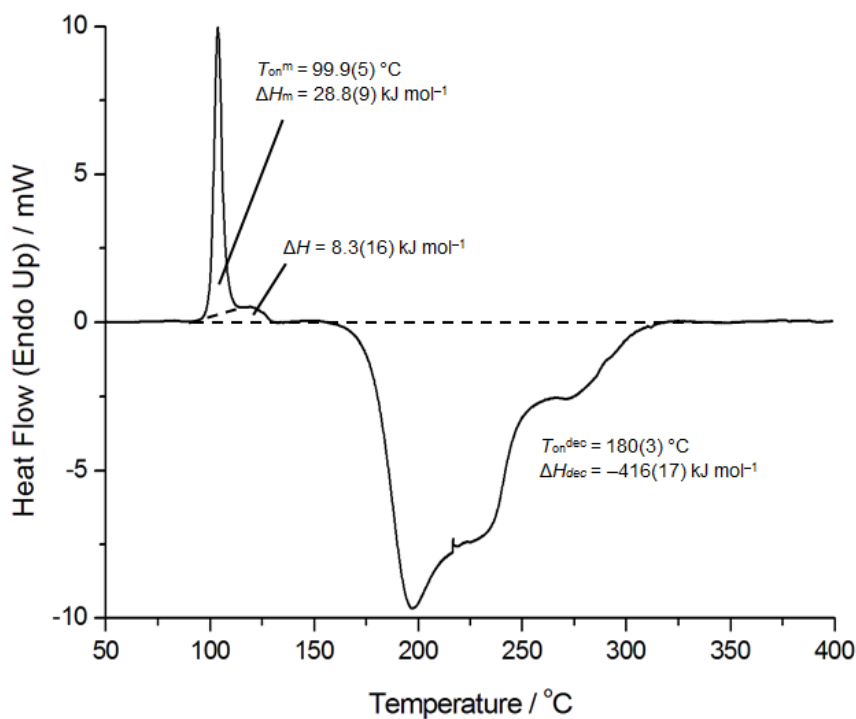


Figure S30. DSC trace of $\text{Sn}(\text{N}_3)_2(\text{pic})_2$ (**3**); heating rate $10 \text{ } ^\circ\text{C min}^{-1}$, nitrogen flow rate 20 ml min^{-1} .

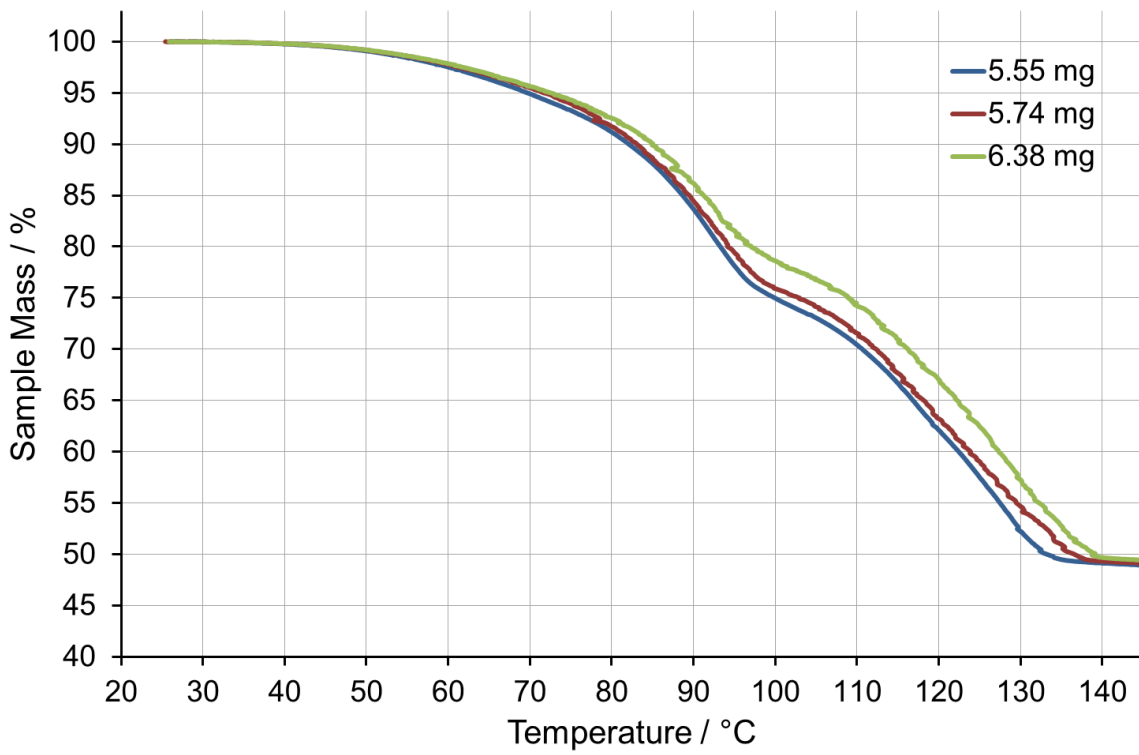


Figure S31. Thermograms (5.55, 5.74, 6.38 mg) of $\text{Sn}(\text{N}_3)_2(\text{pic})_2$ (**3**) showing the mass loss or each equivalent of 4-picoline, leaving behind $\text{Sn}(\text{N}_3)_2$ (**1**). Heating rate $10 \text{ } ^\circ\text{C min}^{-1}$, nitrogen flow rate 20 ml min^{-1} .

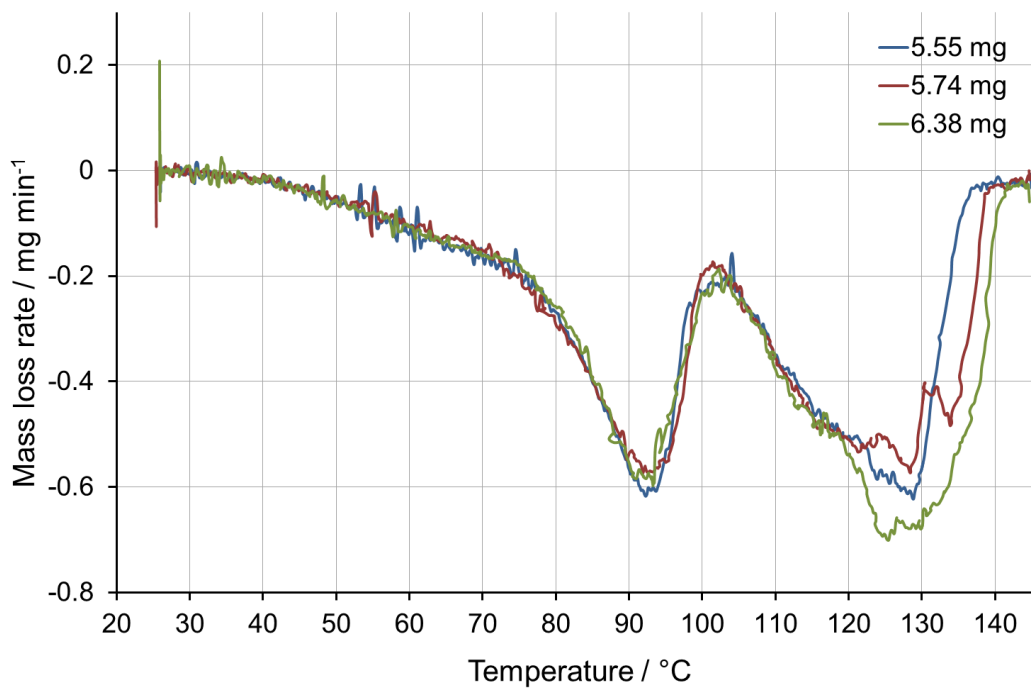


Figure S32. Differential thermograms derived from Fig. S31.

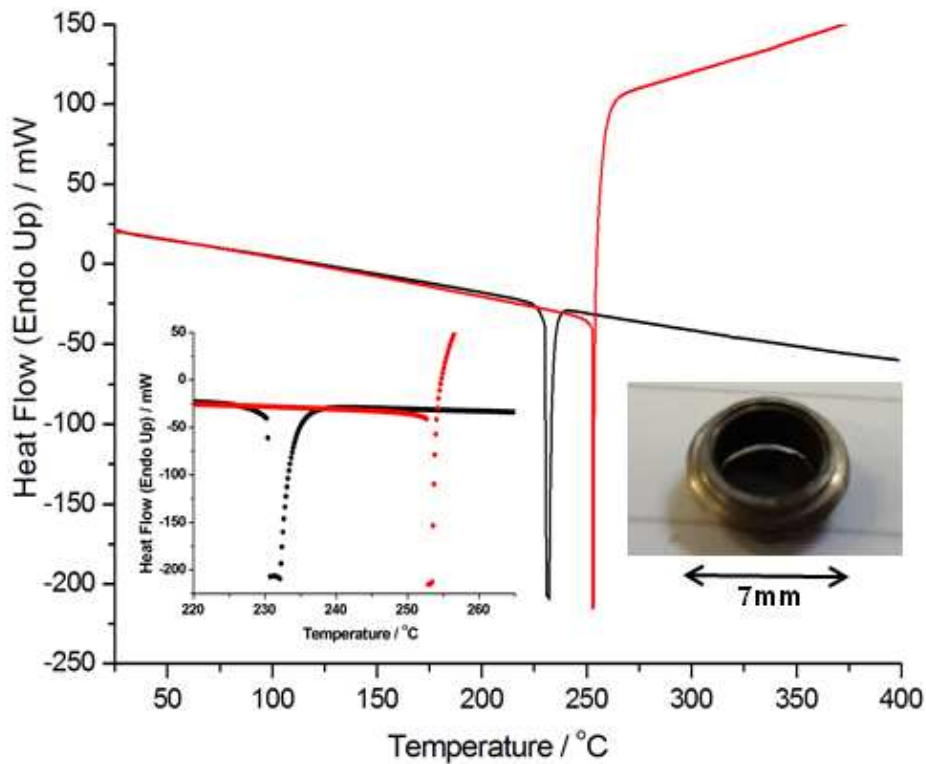


Figure S33. Differential scanning calorimetry traces of tin diazide (**1**) showing an expanded view of the individual data points recorded around the onset of decomposition (detonation); heating rate 10 °C min⁻¹, nitrogen flow rate 20 ml min⁻¹.

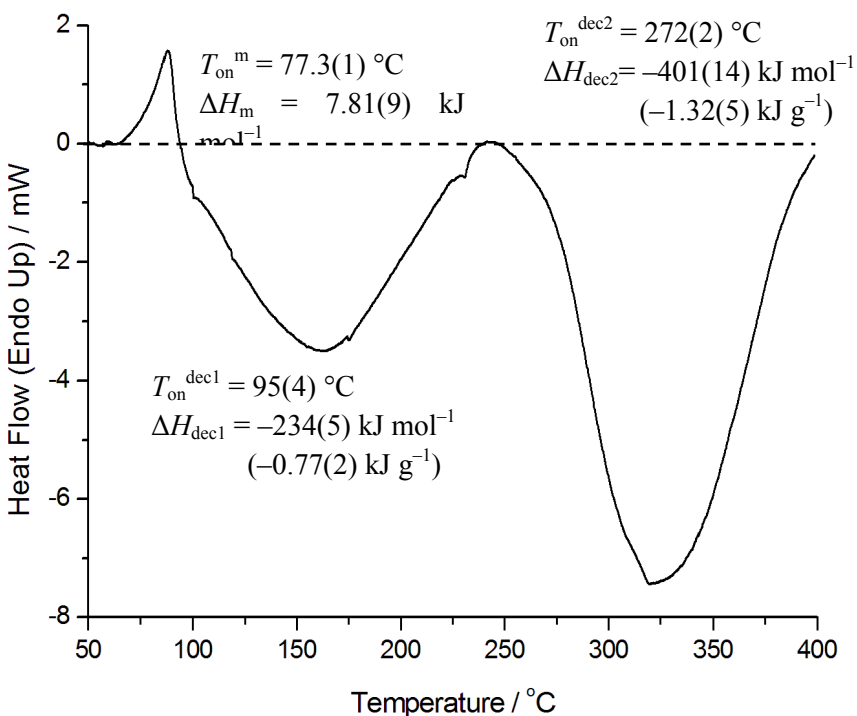


Figure S34. Differential scanning calorimetry trace of **4** showing endothermic melting immediately followed by two-step exothermic decomposition.

8. References to the Literature

1. L. Birkofe and P. Wegner, *Org. Synth.*, 1970, **50**, 107.
2. G. R. Fulmer, A. J. M. Miller, N. H. Sherden, H. E. Gottlieb, A. Nudelman, B. M. Stoltz, J. E. Bercaw, and K. I. Goldberg, *Organometallics*, 2010, **29**, 2176–2179.
3. Bruker *APEX2*, Bruker AXS Inc., Madison, Wisconsin, 2012.
4. Bruker *SAINT*, Bruker AXS Inc., Madison, Wisconsin, 2007.
5. Siemens Area Detector Absorption Correction (*SADABS*), G. M. Sheldrick, 2007.
6. *SHELXS-97*, G. M. Sheldrick, *Acta Cryst. A*, 2008, **64**, 112-22.
7. *Shelxtl*, G. M. Sheldrick, *Acta Cryst. A*, 2008, **64**, 112-22.
8. L. J. Farrugia, *J. Appl. Crystallogr.*, 1999, **32**, 837–838.
9. L. J. Farrugia, *J. Appl. Crystallogr.*, 2012, **45**, 849–854.
10. L. J. Farrugia, *J. Appl. Crystallogr.*, 1997, **30**, 565–565.
11. *DIFFRAC.EVA v3.1*, Bruker AXS Inc., 2010.
12. G. S. Pawley, *J. Appl. Crystallogr.*, 1981, **14**, 357–361.
13. *TOPAS Academic*, A.A. Coelho, 2007.
14. S. J. J. Clark, M. D. Segall, C. J. J. Pickard, P. J. J. Hasnip, M. I. J. Probert, K. Refson,

- and M. C. Payne, *Z. Krist.*, 2005, **220**, 567–570.
- 15. A. Tkatchenko and M. Scheffler, *Phys. Rev. Lett.*, 2009, **102**, 73005.
 - 16. J. P. Perdew, K. Burke, and M. Ernzerhof, *Phys. Rev. Lett.*, 1996, **77**, 3865–3868.
 - 17. J. Vackář, M. Hyt'ha, and A. Šimůnek, *Phys. Rev. B*, 1998, **58**, 12712–12720.
 - 18. J. D. Pack and H. J. Monkhorst, *Phys. Rev. B*, 1976, **13**, 5188–5192.
 - 19. T. H. Fischer and J. Almlöf, *J. Phys. Chem.*, 1992, **96**, 9768–9774.
 - 20. R. L. Licherter and J. D. Roberts, *J. Am. Chem. Soc.*, 1971, **93**, 5218–5224.